The slab-mantle wedge interface of an incipient subduction zone: Insights from the *P-T-D* evolution and petrological characteristics of the Dalrymple Amphibolite, Palawan Ophiolite, Philippines

Gabriel Theophilus V. VALERA[1,*], Tetsuo KAWAKAMI[1], Betchaida D. PAYOT[2]

[1]Department of Geology and Mineralogy, Graduate School of Science, Kyoto University, Kitashirakawa-Oiwake-cho, Sakyo-ku, Kyoto 606-8502, Japan.

[2] National Institute of Geological Sciences, University of the Philippines, Diliman, Quezon City 1101, Philippines

*corresponding author: gtv.valera@gmail.com

Abstract

In this contribution, we present the petrological characteristics and pressure-temperature-deformation (*P-T-D*) history of the Dalrymple Amphibolite in Palawan Island, Philippines. This unit occurs below the residual mantle peridotites of the Palawan Ophiolite composed of interlayered dunite and harzburgite. The Dalrymple Amphibolite is predominantly comprised of high-grade metamafic blocks with minor metasedimentary units surrounded by a highly sheared hybridized matrix (kyanite + Ca-amphibole + biotite + ilmenite ± garnet).

Zr-in-rutile geothermometry and quartz-in-garnet geobarometry of the garnet amphibolite block reveals the *P-T* conditions of the prograde metamorphism from ~625 °C, 11.5 kbar to ~700 °C, 13 kbar. Zr-in-rutile geothermometer and the TZARS geobarometer (clinozoisite + rutile + quartz = anorthite + titanite + H_2O) further indicate comparable peak metamorphic conditions for the amphibolite and epidote amphibolite (~605-710 °C, 10-13 kbar) blocks. Geothermobarometry of the matrix surrounding the blocks reveals similar peak metamorphic conditions of ~700 °C and 13 kbar to the garnet amphibolite blocks. The paleogeothermal gradient preserved in the Dalrymple Amphibolite (~16 °C/km) and its block-in-matrix structure are atypical of metamorphic soles, and are more akin to high-*T* mélange complexes interpreted to have formed during incipient subduction. These *P-T* estimates and its block-in-matrix structure suggest that the Dalrymple Amphibolite likely represents the slab-mantle wedge interface of a young arc complex already transitioning from the much warmer paleogeothermal gradients of the slab-mantle wedge interface when subduction was first initiated.

The similar peak metamorphic conditions constrained in the matrix and the metamafic blocks in the Dalrymple Amphibolite indicate that the matrix-forming deformation started before the sequence reached peak metamorphic conditions at depths of around 45 km. Furthermore, the petrological and geochemical characteristics of this block-in-matrix sequence and the multiple generation of cross-cutting veins reveal the complex processes that occur in the slab-mantle wedge interface of an arc in its infancy. Our results highlight the prevalence of Ca-amphibole and kyanite over phyllosilicates (e.g. chlorite and serpentine) in the mélange matrix, mixing of crustal components

along the slab-mantle wedge interface promoted by multiple deformation events and the ubiquity of fluids throughout its history. Subduction zones with similar geothermal gradients (e.g. warm subduction zones) possibly share these petrological characteristics.

Keywords: Dalrymple Amphibolite, slab-mantle wedge interface, incipient subduction zone, mélange complex

1. Introduction

The boundary between the subducting oceanic lithosphere and the mantle wedge, i.e. slab-mantle wedge interface (also termed subduction channel by Bebout, 2013 and plate interface by Agard et al., 2016, 2018), is a dynamically evolving component of intraoceanic subduction zones. Processes that occur in this interface are thought to control arc magma chemistry (Marschall and Schumacher, 2012; Codillo et al., 2018). Much of the information on the slab-mantle wedge interface beneath a mature arc comes from studies of high P/T type metamorphic terranes (e.g. Locatelli et al., 2019). These studies reveal chaotic mélange complexes that preserve paleogeothermal gradients of 4–10 °C/km (e.g. Guillot et al., 2009; Bebout and Penniston-Dorland, 2016). These complexes are composed of blocks derived from the underthrusting slab and the overlying serpentinized mantle surrounded by a highly sheared, fluid-rich matrix (e.g. Guillot et al., 2009; Bebout, 2013). This matrix represents the mixture of end-member lithologies (sediment, basalt/gabbro, and peridotite) in the slab-mantle wedge interface (e.g. Bebout and Barton, 2002; Marschall and Schumacher, 2012).

The slab-mantle wedge interface during the earliest stages of intraoceanic subduction on the other hand, is sometimes preserved as relatively intact sheets of metamorphic soles that underlie the mantle section of ophiolites. Ophiolites, which are fragments of fossil oceanic lithosphere, allow direct observation of the spatial, temporal and structural relationships of the different sections comprising an oceanic crust and mantle. Studies of metamorphic soles (e.g. Semail Ophiolite, Oman) reveal that these thin sheets of amphibolite- and granulite-facies grade metamorphic rocks preserve much higher geothermal gradients of >20 °C/km and are typically formed within the first 2 Myr of subduction inception (e.g. Soret et al., 2017; Agard et al., 2018).

Less information is however available on the petrological characteristics and metamorphic evolution of the slab-mantle wedge interface as it transitions from a young and hot subduction zone to a mature arc with more hydrous minerals (e.g. chlorite and serpentine) stabilized at depth and marked by cold geothermal gradients (e.g. Guillot et al., 2009). A potential candidate for understanding relatively young island arcs is the Philippine island arc system which preserves a complex history of subduction, rifting, and arc-continent collision (e.g. Yumul et al., 2003). In its western margin, the collision between a nascent arc and the southward drifting North Palawan Continental Terrane (NPCT) led to the emplacement of the Palawan Ophiolite. The Dalrymple Amphibolite, a relatively well preserved high-grade metamorphic block-in-matrix complex, is located at the base of this ophiolite. Earlier works interpret these metamafic blocks as the slab-mantle wedge interface (i.e. metamorphic sole) of the Palawan Ophiolite (e.g. Encarnacion et al., 1995; Keenan et al., 2016).

In this contribution, detailed field characteristics of the metamafic blocks coupled with trace element geothermometry (i.e. Zr-in-rutile geothermometer) and elastic geobarometry (i.e. quartz-in-garnet Raman geobarometer) are used to constrain the pressure-temperature-deformation (*P-T-D*) history of the blocks and the matrix which comprise the Dalrymple Amphibolite. Additional constraints are obtained from conventional geothermobarometry, thermodynamic modelling and fluid inclusion microthermometry. Mineral abbreviations are after Whitney and Evans (2010) except for Ca-amphibole (Camp).

2. Geological Setting

Palawan island is located in western Philippines and forms part of the Palawan Microcontinental Block (PCB). It is divided into two terranes, the North Palawan Continental Terrane (NPCT) and the oceanic South Palawan Terrane (SPT, Fig. 1a). The NPCT was part of the Southeast Asian continental margin from Paleozoic through Mesozoic (Padrones et al., 2017; Cao et al., 2020). During the Eocene to Oligocene, rifting in the Southeast Asian margin resulted to the southward drift of the NPCT and ultimately led to the opening of the South China Sea marginal basin (Yumul et al., 2003; Keenan et al., 2016). The compression due to the southward drift of the NPCT was accommodated by subduction on its southeastern front forming a nascent arc. Some authors argue that

91 the Cagayan de Sulu Ridge (CR in Fig. 1a) is the remnant of this nascent arc (Rangin and Silver, 1991).
92 There is however, a significant difference in the proposed age of subduction initiation based on the
93 igneous crystallization age of the ophiolite (~34 Ma; Encarnacion et al., 1995) and the cooling age of
94 the metamorphic sole (~34 Ma; Keenan et al., 2016) compared to the age of arc magmatism in the CR
95 (~18–16 Ma; Rangin and Silver, 1991). During the Late Oligocene to Early Miocene, the NPCT
96 collided with this nascent arc and segments of the overlying plate were thrusted on top of the continent-
97 derived turbidites as the Palawan Ophiolite (e.g. Keenan et al., 2016). Slivers of this fossil oceanic
98 lithosphere crops out extensively in the central and southern segments of the island and is referred to
99 as the South Palawan Terrane. Questions remain with regard to the presence of another Mesozoic
100 ophiolite exposed in south Palawan and underthrusting the Eocene Palawan Ophiolite in central
101 Palawan (e.g. Muller, 1991; Labis et al., 2020). This work focuses on the Eocene ophiolite exposed
102 in central Palawan (e.g. Encarnacion et al., 1995; Keenan et al., 2016).

103 The Palawan Ophiolite represents a complete ophiolite sequence with basaltic pillow lava flows,
104 isotropic and layered gabbroic and ultramafic cumulates comprising the crustal section and the residual
105 mantle peridotites below (e.g. Dilek and Furnes, 2014). U-Pb geochronology of zircon separates from
106 a plagiogranite associated with the ophiolite revealed the igneous crystallization age of the ophiolite
107 to be 34.1 ± 0.1 Ma (Encarnacion et al., 1995). A thin block-in-matrix complex composed of high-
108 grade metamorphic rocks underlie the interlayers of mostly fresh to moderately serpentinized dunite
109 and harzburgite in the localities of Botoon, Nanad and Dalrymple points (Fig. 1b). This unit is
110 collectively referred to as the Dalrymple Amphibolite (Fig. 1b). Less extensive metamafic exposures
111 also occur further south along Malatgao river in Dumangueña, Aborlan (Fig. 1a; Raschka et al., 1985).
112 The Dalrymple Amphibolite, along with the other ophiolitic lithologies, are thrusted on top of
113 deformed Eocene turbidites referred to either as Panas-Pandian Formation or the Barton Metamorphics
114 (Fig. 1a; Aurelio et al., 2014).

115 Earlier studies on the Dalrymple Amphibolite exposed in Ulugan Bay in central Palawan,
116 estimated the peak *P-T* conditions of its formation at 700–760 °C at a minimum pressure of 9 kbar

using conventional geothermobarometry, i.e. Grt-Camp-Pl-Qz geobarometer and Grt-Bt and Grt-Camp geothermometers (cf. Encarnacion et al., 1995). $^{40}Ar/^{39}Ar$ ages of 34.2 ± 0.5 Ma, 34.2 ± 0.6 Ma and 34.3 ± 0.3 Ma were obtained from two amphibole samples in metamafic blocks and one muscovite from kyanite-chlorite-muscovite schists, respectively (Encarnacion et al., 1995; Keenan et al., 2016). These were interpreted as metamorphic cooling age of the Dalrymple Amphibolite (Encarnacion et al., 1995). Chemical Abrasion Thermal Ionization Mass spectrometry (CA-TIMS) U-Pb dating of oscillatory-zoned zircons from competent pods in the Dalrymple Amphibolite yielded weighted mean ages of 35.242 ± 0.062 Ma, 35.862 ± 0.048 Ma and 35.25 ± 0.15 Ma (Keenan et al., 2016). This was interpreted as the igneous crystallization age of the mafic protolith of the metamafic blocks.

2.1 Field Occurrence

The Dalrymple Amphibolite occurs as a mélange complex with blocks surrounded by a highly sheared matrix in contrast to the relatively coherent sheets that characterize most metamorphic soles (Agard et al., 2016; 2020). Earlier works, based on kinked quartz and kyanite in the metamafic blocks, attributed the mélange-like appearance to a later, 'cold' deformation event that transformed a more coherent metamafic and schist unit (Encarnacion et al., 1995). Several stages of deformation are however possible in these shear zones as described below.

In Botoon point (10.1353°N 118.8133°E; Fig. 1b), the Dalrymple Amphibolite consists of tabular, angular to subrounded blocks up to 15 m in length (Fig. 2a, b). Most blocks are metamafic, with variable amounts of garnet and epidote. Randomly-oriented epidote-veins are locally developed in an amphibolite block but do not continue to the surrounding matrix (Fig. 2c, d). Minor metasedimentary blocks are also observed, including metacherts (i.e. Camp-Czo quartzites) and metacarbonates replaced by Ep amphibolite. The foliation in some blocks is marked by the arrangement of elongate minerals (e.g. amphibole) or the interlayers of quartz-rich and mafic domains dipping gently (~30°) to the SE. The foliation in the blocks is denoted as S1 (e.g. Fig. 2e).

The blocks in Botoon are surrounded by a sheared matrix material occupying the low-lying portions of the exposure (Fig. 2a–d). Two generations of matrix formation defined by the same

assemblage (Ky+Camp+Bt+Grt+Ilm) but distinguished by cross-cutting pervasive foliation directions are observed (matrix 2a and 2b in Fig. 2). In some parts of the exposure, the foliation of the earlier matrix 2a denoted as S2a (e.g. Fig. 2e) are generally subparallel to those of the blocks. Elongate minerals such as kyanite and Ca-amphibole exhibit foliation S2a and a WNW-ESE mineral lineation is observed locally in the kyanite and quartz. In other parts of the exposure, coarse kyanite grains are surrounded by accumulations of ilmenite (Fig. 2f, g). Quartz and Qz-Ky-rich domains occur as deformed lenses (Fig. 2e) arranged subparallel to the foliation of the matrix2a (S2a) and as veins cross-cutting the matrix (Fig. 2h) and the blocks. In some parts of the exposure, the matrix2a is cut by a subsequent melanocratic matrix2b which transformed the earlier formed matrix2a into small autochthonous blocks (Fig. 2i, j). The matrix2b in Botoon have the same mineralogy as the earlier matrix2a but elongate minerals (e.g. Ca-amphibole and kyanite) exhibit distinct foliation, denoted as S2b.

Some of the blocks (e.g. metacarbonates) in Botoon are surrounded by rinds (Ep amphibolite) with concentric foliation and separating the blocks from the matrix. In other blocks, a distinct rind is not observed but progressive changes in mineralogy (e.g. increasing garnet in some metamafic blocks) can be noted towards the contact with the matrix (Fig. 2d). The overlying interlayers of dunite and harzburgite are exposed in the NE side of the exposure.

The contact between the Dalrymple Amphibolite and the mantle section of the ophiolite is best exposed in Nanad (Figs. 1b, 3a). Shear-sense indicators suggest a top-to-the-NW sense of movement (Fig. 3b). Shearing is also more pervasive in Nanad than Botoon. The blocks in Nanad are smaller and have rounded to subrounded corners compared to those in Botoon (Fig. 3c). The matrix2a with Ky+Camp+Bt+Grt assemblage in Botoon is also found as randomly-oriented blocks in this locality (Fig. 3d–e). Amphibolite cut by Qz-Ky veins, also observed in Botoon, occur as blocks in Nanad. These veins abruptly end and do not continue towards the surrounding matrix2b (Fig. 3f, g). In Botoon matrix2b occurs locally, cross-cutting the predominant matrix2a. In Nanad, matrix2b is the dominant matrix type. This matrix2b (Grt+Ky+Camp+Bt+Qz) surrounds metamafic and matrix2a blocks as well

as garnet (0.5–5 mm), peapod-shaped Ca-amphibole (0.5–7 mm) and altered kyanite porphyroclasts. Local S-C fabrics are also exhibited by matrix2b in Nanad.

The metamorphic rocks are most extensively exposed in Dalrymple point (Figs. 1b, 4a). The exposure can be divided to a block-dominated zone in the northwest which occurs proximal to dunite-harzburgite interlayers and a more homogenous amphibolite zone to the southeast (cf. Encarnacion et al., 1995; Keenan et al., 2016). The NW zone consists of interlayered blocks of garnet amphibolites (Fig. 4b, c), metachert quartzite (Fig. 4d) and biotite schists (Fig. 4e) with schistosity dipping moderately (53°) towards the SE. In the northwestern section of the exposure, a resistant quartzite block sits on top of the surrounding Camp-Ky-dominated matrix2a similar to the exposure in Botoon (Fig. 4f). The schistosity of the matrix2a dips gently towards the SE while stretching lineation on S2a (L2 in Fig. 4g) defined by hornblende is N-S. Kyanite crystals are also more extensively replaced by pseudomorphic muscovite compared to other localities (Fig. 4g–h).

Further southeast of the block-dominated zone is a more homogenous, foliated and folded amphibolite, Ep amphibolite sequence (Fig. 4a). The Ep amphibolites are highly sheared (i.e. fine to very fine grained; 0.10–0.25 mm) and generally dip gently towards the SE (Fig. 4i–k). Epidote-rich domains appear as subparallel veins rather than distinct, continuous layers (Fig. 4j, k). The amphibolites commonly occur as elongated pods surrounded by Ep amphibolite and are coarse-grained (Fig. 4l). The sequence is crosscut by quartz veins that are subparallel and in places crosscut the S1 foliation of the Ep amphibolites (Fig. 4j, k). Encarnacion et al. (1995) interpreted the prevalence of Ep amphibolites farther away from the metamorphic-ultramafic contact to signify decreasing metamorphic grade southward although peak *P-T* estimates for the Ep amphibolites are lacking.

The information on samples used in this study are summarized in Table 1 while the deformation stages (D1–D3), veining stages (V1–V3), mineral paragenesis and mineral occurrence based on the field characteristics of the Dalrymple Amphibolite are summarized in Table 2. The timing of matrix formation which surround the blocks relative to the *P-T-D* history of the blocks cannot be constrained solely on field characteristics. In the metamorphic sole of the Semail (Oman) Ophiolite for example,

shearing which isolated and emplaced high-grade metamafic blocks against lower *P-T* metamorphic rocks, occurred late in its *P-T-D* history (e.g. Soret et al., 2017). In the Catalina schists on the other hand, petrological and field characteristics reveal that matrix formation started early at lower grades and the mélange sequence as a whole was subsequently exposed to higher *P-T* conditions along the subduction channel (e.g. Penniston-Dorland et al., 2014; 2018). In the case of the Dalrymple Amphibolite, constraining the *P-T-D* history of the blocks and the surrounding matrix is needed to elucidate the origin of the block-in-matrix sequence as a whole.

The information for the metamafic and metasedimentary blocks are therefore recorded as Stage 1 while those of the matrix are regarded as Stage 2 in Table 2. In the exposures in Botoon and northwest Dalrymple, the first stage of deformation (D1) is preserved as foliation (S1) in the blocks. Deformation events related to the formation of schistosity (S2a) and stretching lineation (L2) in matrix2a is marked as D2a. In Botoon, the start of a subsequent deformation event (D2b) is hinted by the formation of matrix2b which crosscuts the matrix2a (Fig. 2i, j) and follows a distinct foliation direction (S2b). The exposure in Nanad exhibits a more pervasive D2b deformation. Matrix2a occurs exclusively as rounded blocks (Fig. 3d, e) along with the blocks of other rock types which preserve the earliest stage (Stage 1, D1). The surrounding matrix2b is finer-grained (~0.05 mm) than matrix2a, highly foliated (S2b) and locally preserves S-C fabric (S2b and C2b).

Lastly, coarser Stage 1 and Stage 2 minerals comprising both the blocks and the matrix respectively, are partially to completely replaced by finer hydrous minerals in most samples, e.g. kyanite to muscovite and ferromagnesian minerals to chlorite, epidote and actinolite. These replacement minerals also occur as veins which cut through the foliation of the blocks and both matrix2a and 2b. This indicates a final retrograde stage (Stage 3) where the planar veins associated with Stage 3 indicate a late stage deformation event (D3) during Stage 3.

3. Analytical methods

Quantitative analysis of rock-forming minerals and X-ray elemental mapping of thin section samples were conducted using a JEOL JXA-8105 electron probe microanalyzer. Analytical conditions

for quantitative analyses were 15.0 kV acceleration voltage, 10 nA beam current, and 3 μm beam diameter. The counting time for the peak and backgrounds were 30 s and 15 s for Cl, 60 s and 30 s for F, and 10 s and 5 s for other elements. Natural and synthetic minerals were used as standards and ZAF correction was applied. Representative mineral analyses are given in Tables 3 and 4. Estimation of Fe^{3+} in garnet and Ca-amphibole followed Droop (1987) and Schumacher (1991). Analytical conditions for the Zr-in-rutile geothermometry followed that of Zack et al. (2004). Acceleration voltage used was 20.0 kV, 120 nA probe current and a probe diameter of 5 μm to determine both major and trace element concentration of the rutile grains. Elemental mapping was conducted using an acceleration voltage of 15.0 kV, probe current of 60 nA, with either a focused beam or a beam diameter of 3–5 μm. Panchromatic cathodoluminescence (CL) mapping of quartz for Stage 3 was performed at 15.0 kV, 1 nA. All of the analyses in this study except whole-rock geochemical analysis were done at Department of Geology and Mineralogy, Kyoto University.

Elastic geobarometry utilizing shifts in the Raman bands of quartz inclusions in garnet host was employed by determining remnant inclusion pressures (P_{inc}). The Raman shifts were obtained using a laser Raman spectroscopy (JASCO NRS 3100). P_{inc} can be calculated using room temperature (20 ±1 °C) measurements of the shift from the 128, 206, and 464 cm^{-1} Raman bands of quartz inclusions (Δv_{128}, Δv_{206}, and Δv_{464} respectively) and a hydrostatic pressure calibration (Schmidt and Ziemann, 2000; Thomas and Spear, 2018). Spectral interference from the 170–215 cm^{-1} Raman bands of the garnet host can however result in linewidth broadening of the 206 cm^{-1} band while the 128 cm^{-1} band is relatively weak and is not observed in some inclusions (e.g. Thomas and Spear, 2018). The shift of the 464 cm^{-1} band (Δv_{464}) was therefore used to calculate the entrapment isomeke consistent with the method employed in other related studies (e.g. Thomas and Spear 2018). The isomeke represents the *P-T* curve along which fractional volume changes of the host and inclusion are the same and whose instantaneous slope is determined by the ratio of the difference in volume thermal expansion coefficients and compressibility of quartz and garnet (e.g. Angel et al., 2017a, b). The entrapment isomeke was calculated using the freeware EoSFit-Pinc module (e.g. Angel et al., 2017a) applying the

247 equation of state parameters for the curved α-β quartz phase boundary of Angel et al. (2017b) and the
248 Tait equation of state and parameters for garnet from Holland and Powell (2011).

249 Fluid inclusion assemblages associated with Stage 3, were identified by petrography and CL-
250 imaging. Microthermometry was performed using a LINKAM, LK-600 heating and cooling stage. The
251 calibration was performed on synthetic fluid inclusion standards, 10 wt% NaCl solution and pure water.
252 Final ice-melting temperature and total homogenization temperature of the two-phase aqueous fluid
253 inclusions were determined by heating and cooling the fluid inclusions respectively at a rate of 1 °C
254 min^{-1} close to the final temperature. Precision of the microthermometric measurements are ± 0.1 °C
255 for melting and homogenization temperatures. During our heating experiments, no decrepitation was
256 observed.

257 Representative matrix sample B214-10 used for thermodynamic modelling was powdered in a
258 tungsten-carbide mill at Kyoto University and whole-rock geochemical analysis was performed at
259 Bureau Veritas, Perth, Australia. Major-element concentrations were obtained by fused glass bead X-
260 Ray fluorescence (XRF) analysis. Analytical precision based on replicate sample is within 1 % for all
261 elements.

262 **4. Results**

263 **4.1 Petrography and mineral chemistry of blocks**

264 **4.1.1 Garnet amphibolites**

265 The earliest stage of metamorphism and deformation (Stage 1a in Table 2) is preserved in the
266 Grt amphibolite blocks (Fig. 5a, b; Botoon: B213-8, B214-21; Dalrymple: D113-14, D113-15, D113-
267 18). The Grt amphibolite blocks consist mainly of Grt+Camp+Ep(Czo)+Qz with accessory minerals
268 Rt+Ilm+Bt (Table 1). Plagioclase is absent in Grt amphibolite samples from Botoon while it occurs as
269 a major matrix mineral (Pl1b in Table 2) in one block from Dalrymple point (D113-15), and in minor
270 amounts (< 5 vol%) in two Dalrymple point samples (D113-14 and D113-18; Table 1). Secondary
271 minerals such as epidote and chlorite occur as veins and along grain boundaries.

The Grt porphyroblasts in these samples exhibit pronounced concentric compositional zoning marked by increasing pyrope content and Mg# [= Mg/(Mg+Fe^{2+})] and decreasing spessartine content from core (e.g. B214-21 =$Alm_{46-51}Prp_{10-19}Grs_{15-20}Sps_{15-25}$) to rim (= $Alm_{38-41}Prp_{30-35}Grs_{13-15}Sps_{13-17}$; Fig. 5a–d). Stage 1 is therefore subdivided in the garnet core and its inclusion assemblage (Stage 1a) and the garnet rim and matrix assemblage (Stage 1b). Multiphase solid inclusions (MSI) composed of Chl+Ep+Qz+Grt+Rt+Ilm (B213-9; Fig. 5d) occur in the Sps-rich, low Mg# core of some garnet porphyroblasts (Grt1a). The Sps-poor, Mg-rich rim of the garnet porphyroblasts (Stage 1b in Table 2) exhibit textural equilibrium, i.e. sharp boundaries, with the surrounding Ca-amphibole (Camp1b), epidote (clinozoisite), quartz, rutile and ilmenite.

The Grt amphibolite block B214-21 used for geothermobarometry (Tables 1.1 and 1.2) contains garnet porphyroblasts distributed parallel to the arrangement of the long axis of hornblende in the matrix. This arrangement defines the foliation (S1) in the Grt amphibolite blocks (Fig. 5a). S1 foliation is attributed to the deformation (D1) that affected the blocks prior to the block-in-matrix structure formation (Table 2). A quartz-kyanite vein (V1) cuts B214-21 and includes garnet and Ca-amphibole derived from the block. These minerals incorporated in the vein have the same composition and zoning pattern (in the case of garnet) as those in the block (Fig. 5a). There is no reaction zone between the vein and block. Furthermore, local Al-rich domains are observed in this sample where minor amounts of (< 5%) kyanite (Ky1b) and epidote (Czo1b) are in textural equilibrium with the garnet porphyroblasts (Table 2).

The Ca-amphibole (Camp1b) in the Grt amphibolite blocks range from ferrotschermakite to tschermakite with minor magnesiohornblende (Fig. 6a, b). Some Ca-amphibole in the matrix of these blocks show increasing Si, Al and Mg# from the core to the rim (Fig. 6a, b). Other Stage1b Ca-amphibole (Camp1b) grains are replaced along grain boundaries by either actinolite (Camp3) or chlorite (Chl3). Chlorite (Chl1a) inclusions in the garnet core generally have lower Si (= 5.3–5.4 a.p.f.u.) and higher Mg# (= 0.46–0.53) than replacive chlorite (Chl3 in Table 2; Si = 5.9–6.7 a.p.f.u., Mg# = 0.38–0.53) and epidote (Ep3 in Table 2). These replacive chlorite (Chl3) occurs as veins and as secondary minerals surrounding garnet and Ca-amphibole rims (Fig. 5a-c). Muscovite hosted by

299 garnet in the Grt amphibolite blocks (Ms1a; Table 2) have moderate phengite component (Ms1; Si =
300 3.13–3.28 a.p.f.u.) whereas fine mica aggregates (Ms3) are classified as aluminoceladonite (Fig. 6j,
301 k). Plagioclase in some Grt amphibolite blocks have low Ca-content (D113-14 = An_{10-16}, D113-18 =
302 $An_{10–18}$) and some are rimmed by albite (Pl3 = $An_{<5}$; Fig. 6l). An exception to this is the Grt
303 amphibolite block D113-15 composed mostly of Ca-rich plagioclase ($An_{15–24}$). Whole-rock data
304 reveals a gabbroic protolith for this sample (cf. Part 2).

305 Rutile grains in the Grt amphibolite block D113-14 have low Nb and Cr content while those in
306 B214-21 exhibit systematic variability in their chemistry. Rutile grains included in the garnet core
307 (Rt1a in Table 2) of B214-21 have low Zr (Fig. 7) and Nb contents (175–266 ppm; Fig. 6 m). Those
308 enclosed in the garnet mantle and rim have higher Nb concentration, 161–6664 ppm and 720–5606
309 ppm, respectively (Fig. 6 m). These values are comparable to the Nb content of rutile in the matrix
310 (1692-5082 ppm) and those included in Camp1b (587–4760 ppm). These high Nb rutile grains are
311 grouped as Rt1b in Table 2.

312 **4.1.2 Amphibolites**

313 The amphibolite lenses (D113-9; D113-11) hosted in Ep amphibolites in Dalrymple point are
314 composed almost exclusively (~90 %) of coarse Ca-amphibole along with minor amounts of
315 Ep+Pl+Qz+Rt+Ttn (Table 1; Fig. 5e, f). The absence of garnet porphyroblasts in the amphibolite
316 blocks limits the use of mode of occurrence in discriminating between garnet inclusion assemblage
317 (Stage 1a) and the matrix assemblage (Stage 1b). Some of the Ca-amphiboles (Camp1b) in the
318 amphibolites show optical zonation (Fig. 5f) and have dark (low Al_T = 1.55 a.p.f.u., high Mg# = 0.77)
319 cores and brighter (high Al_T = 1.78–1.83 a.p.f.u., low Mg# = 0.72–0.75) rims in BSE images (Fig. 5g).
320 Compared to Camp1b in the Grt amphibolites, the amphiboles in amphibolites are mostly
321 magnesiohornblende and have lower total Al content (Al_T) and higher Si and Mg# (Fig. 6a, b).
322 Actinolite (Camp3 in Table 2) replacing Camp1b is also more common in the amphibolite blocks (Fig.
323 6a, b). The plagioclase (Pl1b) in the amphibolite blocks are An_{2-17} in composition, while epidote
324 (Ep1b) are clinozoisite (= $Ps_{20–22}$). Rutile (Rt1b in Table 2) occurs in small quantities in the
325 amphibolites and is sometimes partially surrounded by titanite (Fig 1.5i inset). Some rutile grains in

the matrix show increasing Zr content towards the rim (Fig. 5i). Rutile in these blocks generally have low Nb content (748–1782 ppm) although some grains in D113-9 have higher Nb concentration (Fig. 6 m).

4.1.3 Epidote amphibolites

The Ep amphibolites in Dalrymple point (D113-2, D113-5; Fig. 5j–n) are fine-grained (~0.2 mm) and consist mainly of Camp1b, Pl1b, Qz1b, and Ep1b (Czo; core = $Ps_{20–29}$; rim = $Ps_{22–27}$) with Rt+Ttn+Bt as accessory minerals (Table 1). Like the Grt amphibolite in Botoon point, the Ep amphibolite blocks in Dalrymple are highly foliated. The foliation (S1), marked by the arrangement of Ca-amphibole (Camp1b), epidote (Ep1b) and biotite (Bt1b) (Fig. 5j–l), is associated to the deformation of the blocks (D1). The Ca-amphibole are mostly tschermarkite-magnesiohornblende and show similar chemical zonation pattern as those in the amphibolite blocks. Ca-amphibole has higher Mg# and lower Al content at the core than the rim (Fig. 6a). Replacement of Camp1b by actinolite (Camp3) is more common in the Ep amphibolites compared to the Grt amphibolites (Fig. 6a-b). The growth of actinolite in some Ep amphibolite samples are linked to late stage quartz veins (V3). In the sample D113-1, replacement of hornblende (Camp1b) by actinolite (Camp3) is more pervasive closer to a V3 Qz-vein (Act zone) which crosscuts its foliation (cf. Section 1.5.3.3). Plagioclase (Pl1) in the Ep amphibolite have low An content (e.g. D113-2 = $An_{7–15}$, D113-5 = $An_{1–12}$) although those in D113-8 are more anorthitic ($An_{16–27}$, Fig. 6l). Similar to the Grt amphibolite sample D113-15, whole-rock data also show a gabbroic protolith for this Ep amphibolite block with An-rich plagioclase (cf. Part 2). Minor biotite (Bt1 in Table 2) in the Ep amphibolites occurs as anhedral interstitial grains (Fig. 5k–l). The Mg# (0.53–0.56) and Ti (0.05–0.11 a.p.f.u.) of Bt1b in the Ep amphibolites are comparable to those in the Grt amphibolite block D113-18 (Mg# = 0.50–0.58; Ti = 0.01–0.11 a.p.f.u.; Fig. 6g). Titanite is also more common in this lithology. Rutile (Rt1b) in the Ep amphibolite records the lowest Nb concentration (<958 ppm; Fig. 6m). Lastly, rutile in the Ep-Bt-Ms schist block sample 215-7 have the highest Nb concentrations ranging from 1.5-6.2 wt.% (Fig. 6m, n).

352 **4.2 Petrography and mineral chemistry of matrix2a and matrix2b**

353 Stage 2 in Table 2 is assigned to the two generations of matrix (2a and 2b) surrounding the
354 blocks of the Dalrymple Amphibolite. The mineral assemblage of matrix2a is highly variable but
355 always includes kyanite (Ky2a) and ilmenite (Ilm2a; Fig. 8a–d). Hornblende (Camp2a), biotite (Bt2a),
356 quartz (Qtz2a) and garnet (Grt2a) are present in most matrix samples but are sometimes absent in other
357 samples (Table 1). Minor chlorite (Chl2a) occurs as local inclusions in kyanite and Ca-amphibole in
358 B214-8 and B214-2G (Table 2). Orthoamphibole is also present in some matrix2a samples (e.g.
359 Oam2a in B214-29; Table 1) coexisting with Ca-amphibole (Camp2a). Accessory minerals include
360 Ap+Rt while secondary minerals, muscovite (Ms3), chlorite (Chl3) and epidote (Ep3), are similar to
361 those in the blocks (Fig. 8).

362 The foliation trend of the matrix2a (S2a) is typically identifiable from the arrangement of
363 elongate minerals Ky2a and Camp2a as well as Bt2a when present (e.g. B214-2G; Fig. 8e, j). Garnets
364 in matrix2a are typically euhedral, fine-grained (Grt2a, < 50 μm) and are often included in larger
365 matrix2a minerals (e.g. Ky2a in B214-14; Fig. 8h, i). The matrix2a sample B214-2G from Botoon
366 preserves a unique mineral assemblage of coarser Grt2a (~5 mm), staurolite (St2a), kyanite (Ky2a),
367 Ca-amphibole (Camp2a) and biotite (Bt2a) (Fig. 8j, k). The foliation (S2a) marked by the elongate
368 minerals in this sample is a clear evidence of the D2a deformation that affected the matrix2a.

369 Matrix2b in Botoon point is associated with thin shear zones that cut earlier matrix2a (e.g. Fig.
370 8a–c). In this locality they consist of the same minerals (Ky2b, Camp2b, Oam2b in Table 2) as the
371 matrix2a that they transect but follow a distinct foliation direction (S2b). Their cross-cutting
372 relationship and the different foliation trend of matrix2b corresponds to a later deformation event
373 (D2b) during Stage 2. In Nanad point, matrix2b is more dominant and D2b is apparently more
374 pervasive. Matrix2b is largely composed of biotite (Bt2b) and quartz which surround garnet (Grt2a)
375 and hornblende (Camp2a) porphyroclasts. Thin overgrowths of Ca-amphibole (Camp2b) and garnet
376 (Grt2b) surround the margins of some Camp2a and Grt2a porphyroclasts, respectively (Fig. 8o, p;
377 Table 2).

S-C fabrics are observed in this sample (Fig. 8l). The S-plane (S2b) is marked by the arrangement of Ca-amphibole (Camp2a) and kyanite (Ky2a) porphyroclasts and the surrounding biotite (Bt2b in Fig. 8m–p). The C-plane (C2b, Fig. 8l–n), which still contains minor biotite, is largely composed of replacive chlorite (Chl3) and muscovite (Ms3; Fig. 8n). Some of the Chl3 and Ms3 in the C-plane (C2b) are arranged parallel to its direction while others are oriented randomly. Both chlorite and muscovite also replaces the Bt2b in the S-plane in matrix2b (Fig. 8 m, n).

Garnet (Grt2a in Table 2) in the matrix2a (Fig. 6c) lack the pronounced chemical zonation observed in the garnet porphyroblasts in the blocks (Fig. 5c, d). The Grt2a that do exhibit subtle zonation, preserve increasing Prp and Mg# (e.g. B214-6) from the core ($Alm_{36}Prp_{28}Grs_{17}Sps_{19}$; Mg# = 0.44) to the rim ($Alm_{36}Prp_{32}Grs_{16}Sps_{16}$; Mg# = 0.47). The Grt2a garnet grains also generally record higher Mg# (e.g. B214-2G, Mg# = 0.44–0.47) and slightly lower Ca content (e.g. B214-2G = $Grs_{16–19}$) compared to the garnet porphyroblasts in the Grt amphibolite blocks (e.g. Grt1a-b in D113-18, Mg# = 0.30–0.38; $Grs_{18–23}$). An exemption to this general distinction between garnet in the blocks (Grt1) and in matrix2a (Grt2a) is the rim stage (Grt1b) of the Grt amphibolite blocks in Botoon. These Grt1b in Botoon blocks (e.g. B214-21) also record comparably high Mg# (Grt1b in B214-21, Mg# = ~0.41; Grt1b in B213-8, Mg# = 0.40–0.47) and low Ca content (Grt1b in B214-21, $Grs_{13–15}$; Grt1b in B213-8 = $Grs_{8–16}$) as the Grt2a.

Calcic amphibole in matrix2a (Camp2a in Table 2) is classified as tschermakite to magnesiohornblende (Fig. 6d, e). Ca-amphibole (Camp2a) exhibits a generally narrow range of Mg# (0.72–0.78) which is comparably higher than Ca-amphibole in the blocks (Camp1) at a given Si content. Amphibole in samples with two matrix generations, i.e. matrix2a and matrix2b such as B214-29 (Fig. 8a–c) and N215-3 (Fig. 8l–n), exhibit comparable compositions in terms of Al_T, Mg# and Si (Fig. 6d, e). In sample B214-29, the hornblende (Camp2a) are relatively Cr-rich (matrix2a = 0.12–1.3 wt.% Cr_2O_3; matrix2b = 0.12–0.37 wt.% Cr_2O_3) compared to those in blocks (Camp1 < 0.1% wt.% Cr_2O_3). Orthoamphibole is found exclusively in the matrix surrounding the blocks and mostly ranges from gedrite to anthophyllite (Leake et al., 1997). Like the Ca-amphiboles, the orthoamphiboles in matrix 2a and 2b have the same composition (Mg# and Si; Fig. 6f). Kyanite (Ky2) in the matrix sample

B214-29 is also relatively Cr-rich (matrix2a = 0.710 – 2.17 wt.% Cr_2O_3; matrix2b = 0.01–0.67 wt.% Cr_2O_3) compared to other samples. The matrix2a sample B214-5 contains kyanite (Ky2a) grains which are surrounded by fine-grained muscovite (Ms3) connected by radially-oriented healed fractures. These fluid-inclusion bearing fractures will be utilized to estimate the *P-T* conditions for the growth of replacive minerals (i.e. Ms3) during Stage 3. Biotite (Bt2a, b; Fig. 6g) and chlorite (Chl2a; Fig. 6h) in the matrix are also generally more Mg-rich compared to the blocks.

4.3 Geothermobarometry

4.3.1 *P-T* estimate for Stage 1

The Zr-in-rutile geothermometry which utilizes rutile grains coexisting with quartz and zircon (Tomkins et al., 2007) was employed on the metamafic blocks of the Dalrymple Amphibolite and the surrounding Ky+Camp+Bt+Ep+Grt matrix2a. Rutile grains included along with zircon and quartz in the core (Stage 1a) and rim (Stage 1b) of garnet porphyroblasts in sample B214-21 (Fig. 5a–c) were used to estimate *T* condition preserved in the Grt amphibolite blocks (Fig. 9) (e.g. Suzuki and Kawakami, 2019). Rutile grains in the garnet core (Stage 1a) have lower Zr concentrations (170–266 ppm) compared to inclusions in the garnet rim (422–540 ppm Zr; Stage 2b; Fig. 5c). Those included in Ca-amphibole (281–540 ppm Zr) and in the matrix (266–540 ppm Zr) exhibit the same maximum Zr concentrations as the rutile grains included in the garnet rim. Rutile grains in the Grt amphibolite blocks from Dalrymple point (D113-14 = 311–551 ppm Zr, D113-18 = 329–689 ppm Zr) record a similar range of Zr concentration (Fig. 7).

Several factors may result to lower Zr concentration in rutile which may cause the underestimation of peak *T* conditions. These range from primary processes (e.g. timing of rutile formation relative to *P-T* path) to secondary processes such as retrograde rutile growth and diffusive loss of Zr from rutile during cooling (Penniston-Dorland et al., 2018). In contrast, conditions such as absence of quartz in equilibrium with rutile observed in B214-2G garnet inclusions could result to higher Zr concentration in rutile (Tomkins et al., 2007). Penniston-Dorland et al. (2018) suggested the use of “Mean Maximum Zr-in-rutile” along with textural constraints in interpreting and estimating peak metamorphic conditions. This method was adopted in this study in selecting rutile analysis used

for geothermometry. The rutile grains in the metasedimentary sample D215-7 have very high Nb content (>17,000 ppm) which may have possibly affected its crystal structure (Zack et al., 2004). The Zr content of these rutile grains were therefore not used to estimate *T* conditions.

In the Dalrymple Amphibolite blocks, rutile grains in the matrix (e.g. D113-5 = 348–415 ppm) show maximum Zr concentrations similar to or slightly higher than those which occur as inclusions (e.g. D113-5 = 237–311 ppm). There is no significant difference in the Zr concentration between rutile surrounded by titanite and those without titanite (e.g. D113-8; D113-5). Rutile grains in the Ep amphibolites and amphibolites in Dalrymple show slightly lower Zr concentration than those in the Grt amphibolites but the corresponding difference in peak *T* are small (< 25 °C). The Ep amphibolites in Botoon also have the same Zr concentration as the Grt amphibolites, indicating the stability of epidote at peak *P-T* conditions.

The three Raman bands of quartz inclusions in garnet, i.e. 128, 206 and 464 cm^{-1}, are all shifted towards higher wavenumbers compared to the quartz crystal standard. Replicate analysis showed that the broad 206 cm^{-1} Raman band ($\Delta\nu_{206}$) has the highest variation (n = 84; 2σ = 8 cm^{-1}) while readings of the shifted 464 cm^{-1} ($\Delta\nu_{464}$) band are more precise (n = 84; 2σ = 1.8 cm^{-1}). Quartz inclusions are more abundant at the garnet core (Stage 1a) compared to the rim (Stage 1b). Those at the core have $\Delta\nu_{464}$ = 2.94 ± 0.58 cm^{-1} (n = 16; P_{inc}= 3.29 ± 0.7 kbar using Schmidt and Ziemann, 2000) while the 464 cm^{-1} band of the quartz inclusions at the rim are shifted $\Delta\nu_{464}$ = 2.8 ± 0.65 (n = 8; P_{inc} = 3.14 ± 0.7 kbar using Schmidt and Ziemann, 2000). Other quartz inclusions are either near fractures resulting to lower Raman shifts or are adjacent to other inclusions.

The combined results of Zr-in-rutile geothermometer (Tomkins et al., 2007) and quartz-in-garnet geobarometer (Schmidt and Ziemann, 2000; Angel et al., 2017a, b) applied to inclusions in the garnet porphyroblasts constrain the *P-T* conditions preserved at the garnet core (Stage 1a: ~625 ± 25 °C, 11.5 ± 1.0 kbar) and the garnet rim (Stage 1b: ~700 ± 13 °C, 13 ± 0.5 kbar) of the Grt amphibolite block B214-21 (Fig. 9). The peak *P-T* conditions of other Grt amphibolite blocks from Dalrymple point were constrained by applying the Grt+Camp+Pl+Qz geobarometer (Kohn and Spear,

458 1990) using the garnet rim and matrix assemblage (Grt1b+Camp1b+Pl1b+Qz1b) coupled with Zr-in-
459 rutile geothermometry of rutile grains in the matrix (Rt1b) and included in Ca-amphibole (Camp1b)
460 and garnet rim (Grt1b). The obtained *P-T* condition of ~700 ± 45 °C at 13.2 ± 0.9 kbar (D113-14) and
461 710 ± 40 °C at 11.9 ± 1.3 kbar (D113-18) are comparable to the Stage 1b of B214-21. Note that the *P*
462 obtained for the Grt amphibolite block D113-14 are slightly above the pressure range (2.8–13 kbar) to
463 which the geobarometer of Kohn and Spear (1990) are calibrated.

464 Zr-in-rutile geothermometer was also applied to rutile grains in the matrix and included in Ca-
465 amphibole in representative Ep amphibolite (D113-2) and amphibolite blocks (D113-9). The Zr
466 concentration of these rutile grains, 237–415 ppm for D113-2 and 174–525 ppm for D113-9, are
467 comparable to the range of values in the Grt amphibolites. There are also no systematic differences in
468 the Zr concentration of rutile grains of different texture, i.e. matrix vs inclusion and with or without
469 titanite envelop (Fig. 7) although some coarse rutile grains show increasing Zr concentration towards
470 the rim (Fig. 5i). Peak *P* was estimated for the Ep amphibolites and amphibolites by calculating the
471 position of the equilibria: 3 An+ 2 Czo + Rt + Qz = 3 An + Ttn + H_2O (TZARS; Kapp et al., 2009)
472 using the prograde rim of the corresponding minerals, i.e. albitic rims of plagioclase were not
473 considered. The aH_2O was assumed to be high (= 0.95) based on the absence of calcite in the samples
474 which contain Pl+Czo+Ttn and on the results of previous works (Kapp et al., 2009; Picazo et al., 2019).
475 If the actual aH_2O is less than assumed, the calculated position of TZARS equilibria represent the
476 minimum pressure value for these samples. A decrease in the aH_2O of 0.1 (= 0.85) for example
477 increases the *P* by 0.15 kbar whereas a value of aH_2O = 1 lowers the calculated *P* by 0.07 kbar. The
478 constrained *P-T* conditions for the Ep amphibolite (D113-2: ~660 ± 42 °C at 11.4 ± 1.1 kbar) and
479 amphibolite (D113-9: ~616 ± 29 °C at 10.4 ± 0.9 kbar) blocks are within the range of those obtained
480 for the Grt amphibolite blocks albeit slightly lower with respect to *T* and *P* (Fig. 9).

481 **4.3.2 *P-T* estimate for Stage 2**

482 Zr-in-rutile geothermometer and quartz-in-garnet geobarometer were also applied to the
483 matrix2a sample B214-14. Rutile inclusions in kyanite (Ky2a), and quartz hosted in garnet (Grt2a)
484 which are in turn included in Ky2a were used (Fig. 8e–i). The Grt2a (= $Alm_{35–36}Prp_{28–32}Grs_{16–19}Sps_{16–}$

485 $_{19}$) in this sample are fine-grained and do not preserve clear zonation (Figs. 6c; 8i). The rutile grains
486 have high Zr concentrations (400–614 ppm). The 464 cm^{-1} Raman band of quartz inclusions in the
487 garnet are also shifted $\Delta\nu_{464}$ = 3.04 ± 0.53 (n =12; P_{inc} = 3.41 ± 0.6 kbar). Using these values, the *P-T*
488 condition preserved in this matrix2a sample (= ~700 ± 16°C, 13 ± 0.9 kbar) are obtained, which is
489 comparable to the rim stage of the metamafic blocks (Fig. 9).

490 **4.4 Microthermometry of secondary fluid inclusions and *P-T* estimate for Stage 3**

491 Low-*T* retrograde overprint is observed in blocks and matrix samples of the Dalrymple
492 Amphibolite. In the matrix2a in sample B214-5, kyanite (Ky2a) grains surrounded by fine-grained
493 muscovite (Ms3) are connected by radially oriented healed fractures (Fig. 10a–c). These fractures
494 appear as thin nonluminescent lines compared to the host quartz in CL maps (Fig. 10c). The healed
495 fractures contain two-phase aqueous fluid inclusions apparently related to the formation of the fine-
496 grained muscovite pseudomorphing kyanite (Fig. 10b). Variation in the homogenization temperatures
497 of the retrograde, secondary fluid inclusions are relatively narrow (T_H = 151.8 ± 17 °C; Fig. 10d). The
498 salinity of these fluid inclusions range from 1.82–6.95 wt.% NaCl equivalent using the formula of
499 Bodnar (1993). Bulk density (= 0.94–0.96 g/cm^3) was calculated for these H_2O-NaCl fluid inclusions
500 following Steele-MacInnis et al. (2012). These earlier fractures are transected by later stage fractures
501 which appear as thin subparallel non-luminescent features in the CL maps (Fig. 10c).

502 The subparallel quartz-veins cutting the Ep amphibolite exposure in Dalrymple point (Fig. 4f,
503 g) appear related to hornblende replacement by actinolite (Camp3 in Table 2). In sample D113-1,
504 compositional maps reveal progressively increasing Si, Ca, Mg# and decreasing Na, K and Al towards
505 the quartz vein, i.e. increasing actinolite component (Fig. 10f, g). Hornblende grains closest to the
506 veins (0–10 mm; Act zone in Fig. 10f–g) are completely to almost completely replaced by actinolite
507 (Fig. 10h) whereas farther from the vein (Camp zone in Fig. 10f, g), actinolite occur only along grain
508 boundaries forming irregular networks (Fig. 10i). Later discordant potassium feldspar-veins transect
509 both Act and Camp zones.

510

4.5 Pseudosection modeling

The pseudosection modeling for matrix2a (B214-10; Fig. 11) was done in the Na_2O-MnO-CaO-K_2O-FeO-MgO-Al_2O_3-SiO_2-H_2O-TiO_2 (NMnCKFMASHTO) system using Theriak-Domino (ver 4.2.2017; de Capitani and Brown, 1987, de Capitani and Petrakakis, 2010). The sample shows low degree of Stage 3-related metamorphism, and the peak metamorphism assemblage is largely preserved. The updated database of Holland and Powell (2011) and the activity-composition (*a-x*) relations of Green et al. (2016) for metamafic rocks were used following Jørgensen et al. (2019). H_2O-fluid was included in all assemblages.

The pseudosection for the matrix2a sample B214-10 (Fig. 11) well reproduced the observed Stage 2a mineral assemblage (Camp+Grt+Ky+Ilm+Bt+Mag) within the red *P-T* field (Table 1): Absence of chlorite is predicted over ~650 °C, which constrains the lower *T* limit of the observed stage 2a mineral assemblage. Hornblende is predicted to be stable from ~550–750 °C coexisting with garnet and kyanite among others. Absence of evidence for partial melting in B214-10 constrains the higher-*T* limit. Kyanite limits the minimum *P* recorded in this matrix2a sample. The peak *P-T* conditions modelled through pseudosection is comparable to that obtained using geothermobarometric techniques (Fig. 9).

5. Discussion

5.1 *P-T-D* history of the Dalrymple Amphibolite

Application of Zr-in-rutile geothermometer (Tomkins et al., 2007) and quartz-in-garnet Raman geobarometer (Schmidt and Ziemann, 2000; Angel et al., 2017a, b) to the Grt amphibolite block, B214-21, successfully determined the prograde *P-T* path (~625°C, 11.5 kbar to ~700°C, 13 kbar) that the blocks experienced (Fig. 9). This prograde path is consistent with the garnet zonation, i.e. increasing pyrope and decreasing spessartine content (Fig. 5c, d). The Chl+Ep+Qz+Ms MSI preserved in the core of some garnet porphyroblasts in the blocks (Fig. 5d) also reflect the transition from Ep amphibolite facies to high-pressure amphibolite facies. Considering the high variance of these

lithologies, the use of trace element geothermometry and elastic geobarometry as successful ways of constraining *P-T* conditions is highlighted in this study.

The net-transfer reaction geobarometer, TZARS equilibria (Kapp et al., 2009), provided additional *P-T* constraints on the Ep amphibolites (Fig. 9). This revealed comparable peak metamorphic conditions with the Grt amphibolites in contrast to previous hypothesis (Fig. 9; cf. Encarnacion et al., 1995). Earlier works inferred a mid-oceanic ridge basalt (MORB) protolith for much of the metamafic blocks of Dalrymple point (Keenan et al., 2016). Considering the same MORB protolith and since the peak *P-T* conditions are similar for the Grt amphibolites and Ep amphibolite, the prevalence of epidote in the latter type can possibly be attributed to earlier modification of the basaltic protolith (i.e. Ca metasomatism) relative to typical MORB (Wei and Duan, 2018). The randomly-oriented epidote veins cutting the amphibolite block in Botoon (Fig. 2c) and Dalrymple further support Ca metasomatism of some metamafic blocks. Modifications in the chemistry of basaltic rocks formed in spreading centers, especially in terms of Ca, Na and Mg, is prevalent during hydrothermal alteration (e.g. Seyfried et al. 1988). Whole-rock data also reveal the CaO content of Ep amphibolites to be higher at a given FeO/MgO ratio than the Palawan Ophiolite basalts (Part 2). The same scenario has been documented in other ophiolites (e.g. epidosites in Semail; Gilgen et al., 2016) and greenstone belts (Starr and Pattison, 2019). The pre-D1 modification of the Ep amphibolites is suggested by the similar fine-grained texture and foliation trend shared by the epidote-rich and epidote-poor domains of the amphibolites in Dalrymple (Fig. 4j–k). The random orientation of epidote veins cutting the metamafic blocks in Botoon furthermore suggest that Ca-metasomatism of the metamafic blocks persisted during prograde metamorphism, i.e. subduction of the slab (Fig. 2c).

Compared to Grt amphibolite blocks, garnet in the matrix2a (Grt2a) does not exhibit pronounced zonation. The single *P-T* condition constrained on matrix2a (~700°C, 13 kbar) is essentially the same as the peak conditions preserved in the blocks. This indicate that the matrix-forming deformation (Stage 2, D2a) likely started *en route* towards peak *P-T* conditions at depths of around ~45 km using the density values of Jagoutz and Behn (2013). Pseudosection modelling further supports that the dominant mineral assemblage which comprise the matrix2a, i.e. Ca-amphibole,

563 garnet, biotite, kyanite, and ilmenite, were stable at relatively high *P-T* conditions (Fig. 11) comparable
564 to the peak metamorphic conditions of the blocks determined by geothermobarometry (Fig. 9). This
565 suggests that the unique bulk composition of the matrix2a was largely fixed prior to reaching peak
566 metamorphic conditions. Consequently, the deformation of the blocks (D1) and matrix2a (D2a; Table
567 2) may have occurred continuously as the whole mélange complex was being transported towards
568 greater depths (i.e. prograde path in Fig. 9). In the Catalina Schist, California, the formation of the
569 block-in-matrix structure is considered to have also started at lower *P-T* (i.e. blueschist facies) and the
570 block-in-matrix complex was metamorphosed together towards higher grades, i.e. amphibolite facies
571 (e.g. Penniston-Dorland et al., 2014; 2018).

572 Subsequent deformations (D2b) possibly took place in the mechanically-weak shear zone.
573 Although the specific *P-T* conditions of D2b stage cannot be constrained, matrix2b has similar
574 mineralogy as matrix2a (Camp + Ky + Oam + Bt) in Botoon where development of matrix2b is still
575 weak. Hornblende in matrix 2a and 2b are also chemically identical including in Al_T, Mg# and Ti
576 content which are often used as proxies for *P* and *T* (Fig. 6d-e; Garcia-Casco et al., 2008). Therefore,
577 it is likely that D2b started at similar *P-T* condition as D2a. In Nanad matrix2b is more dominant and
578 consist of finer-grained matrix assemblage of Bt-Qz and thin overgrowths surrounding some garnet
579 and Ca-amphibole porphyroclasts (Fig. 8l–p). Both the matrix2a and 2b are further replaced by chlorite
580 (Chl3) and muscovite (Ms3) assemblage with some grains oriented parallel to the C-plane (C2b) in
581 sample N215-3 (Fig. 8l–p). The prevalence of Ms3, Chl3 and albite (Pl3) during Stage 3 suggests that
582 these replacive minerals grew at lower *P-T* conditions within the Ms+Qz stability field, compared to
583 the other stages (Stages 1, 2) and is likely promoted by fluid migration as the sequence was being
584 exhumed towards lower *P-T* conditions (Figs.10, 12). These fluids possibly utilized pre-existing
585 foliations (S2b and C2b) as their pathways.

586 The *P-T* conditions constrained for the Stage 3 retrograde metamorphism (~600 °C, 8 kbar)
587 using fluid inclusion microthermometry is the final step in the *P-T-D* history of the Dalrymple
588 Amphibolite. Considering that the Ms+Qz-in curve of the matrix2a sample is used, its intersection
589 with the isochore of the fluid inclusions correspond to the maximum *P-T* of Stage 3 (Fig. 12a). The

590 growth of hydrous replacement minerals may have happened at lower *T* within the Ms+Qz stability
591 field and along the isochore line depending on the timing of the infiltration of saline fluids.
592 Nonetheless, the location of the calculated isochore with its low d*P*/d*T* slope clearly support a
593 clockwise *P-T* path for the Dalrymple Amphibolite (Fig. 12). This is consistent with the observation
594 that actinolite, not glaucophane, replaced the hornblende both in the blocks (Camp1) and in the matrix
595 (Camp2). The veins associated with Stage 3 (V3; Fig. 10e–i) suggest that this low *P* and *T* retrograde
596 metamorphism and deformation event (Stage 3, D3) postdating peak metamorphic conditions are
597 likely related to the exhumation of the metamorphic sole together with the ophiolite. Similar clockwise
598 *P-T* path and deformation sequences have been reported from the Semail ophiolite (e.g. Soret et al.,
599 2017).

600 **5.2 The Dalrymple Amphibolite: slab-mantle wedge interface of an infant arc**

601 Different models have been invoked to explain the higher *T/P* gradients in the slab-mantle
602 wedge interface during incipient subduction compared to mature arcs. These warmer conditions are
603 typically recorded in metamorphic soles with their inverted thermal gradients. Current models to
604 explain these characteristics of metamorphic soles are as follows: 1. Sequential underplating of rocks
605 metamorphosed at different grades and different times being juxtaposed together to result in an
606 apparent inverted temperature gradient (e.g. Wakabayashi, 2017); 2. Post metamorphic flattening and
607 lateral attenuation resulting to a condensed metamorphic gradient (e.g. Cowan et al., 2014); 3. Shear
608 heating producing high-grade tectonites in major shear zones documented in the Tsiknias Ophiolite,
609 Greece (Lamont et al., 2020); 4. Flow of hotter asthenospheric mantle during forearc rifting; and 5.
610 The thermal conduction between a warm overriding mantle and the uppermost section of the
611 subducting slab (e.g. Hacker 1990; Agard et al., 2018).

612 Radiometric dating of plagiogranites associated with the Palawan Ophiolite reveals an Early
613 Oligocene (~34.1 Ma; Encarnacion et al., 1995) to Late Eocene age (~40.01 Ma; Dycoco et al., 2021).
614 This is similar to the reported cooling age of the Dalrymple Amphibolite from Ar-Ar dating of
615 amphibole and mica separates (~34.2 Ma; Encarnacion et al., 1995). The synchronous age of the
616 ophiolite and Dalrymple Amphibolite, the comparable peak *P-T* conditions preserved in different

617 blocks and matrix units, and its block-in-matrix occurrence are distinct from typical metamorphic soles
618 which generally consist of relatively intact sheets recording inverted thermal gradient (van Hinsbergen
619 et al., 2015). Such distinct characteristics rule out sequential underplating of diachronously
620 metamorphosed units and post-metamorphic flattening and lateral attenuation for the Dalrymple
621 Amphibolite. Shear heating has been invoked to explain the high *T/P* preserved in the metamorphic
622 sole of the Tsiknias Ophiolite whose cooling age is ~90 Myr younger than the overlying ophiolite
623 (Lamont et al., 2020). In contrast to the Tsiknias Ophiolite, the similar age of the Palawan Ophiolite
624 and Dalrymple Amphibolite supports a spreading center-turned-subduction zone model similar to the
625 Semail Ophiolite (e.g. Rioux et al., 2016). The extensive block-in-matrix structure of the Dalrymple
626 Amphibolite furthermore indicates that deformation was likely not restricted in a single shear zone
627 between the subducting slab and the hanging wall as in the Tsiknias Ophiolite (Lamont et al., 2020).
628 The thermal conduction model wherein the heat from the young and hot overlying mantle, possibly
629 coupled by upwelling asthesnospheric mantle during forearc rifting, may have caused the
630 metamorphism of the slab-mantle wedge interface now preserved as the Dalrymple Amphibolite.

631 Compared to a developed subduction zone, the residual heat of the overlying mantle peridotites
632 during early subduction is significantly warmer (Hacker, 1990; Agard et al., 2018). This heat bakes
633 the crustal lithologies of the subducting slab and prevent the stabilization of serpentine in the overlying
634 mantle. Deformation in incipient subduction is accommodated by weaker lithologies, i.e. sediments
635 (e.g. Agard et al., 2016). Unlike most metamorphic soles however, the *P-T-D* history of the Dalrymple
636 Amphibolite reflects the petrological characteristics of a cooler slab-mantle wedge interface (Fig. 12a).
637 Due to its close association with the ultramafic section of the Palawan Ophiolite and its limited
638 exposure, the Dalrymple Amphibolite has been regarded as a typical metamorphic sole formed during
639 the first million year of subduction initiation (Encarnacion et al., 1995; Keenan et al., 2016). The
640 comprehensive investigation on the *P-T-D* history of its lithologies in this study suggest key
641 differences with typical metamorphic soles.

642 The peak *T* obtained for the block and matrix by Zr-in-rutile geothermometery are generally
643 comparable to that obtained by conventional geothermometers for the Dalrymple Amphibolite (cf.

644 Encarnacion et al., 1995). These values are lower than the peak *T* of other ophiolites (e.g. Semail
645 ophiolite; Soret et al., 2017). The peak *P* values are however significantly higher than other
646 metamorphic soles (e.g. Semail ophiolite; Figs. 9; 12a). The paleogeothermal gradient preserved in
647 the Dalrymple Amphibolite (~16 °C/km) and its block-in-matrix structure are atypical of metamorphic
648 soles but are also warmer than a developed subduction channel underlying a mature arc (Fig. 12a).
649 This intermediate gradient preserved in the Dalrymple Amphibolite and its block-in-matrix occurrence
650 are more comparable to early subduction high *T* mélanges or the high *T* eclogites of Agard et al. (2018).
651 This suggest that the Dalrymple Amphibolite may correspond to the slab-mantle wedge interface of a
652 young subduction complex already transitioning from the much warmer conditions when subduction
653 was first initiated. Compared to metamorphic soles which are interpreted to have formed within 2 Myr
654 from subduction initiation (e.g. Soret et al., 2017), the cooler conditions of this transitional period may
655 be reached within 2–5 Myr (Agard et al., 2018). We can therefore use the characteristics of this
656 mélange complex, that is the Dalrymple Amphibolite, to investigate the petrological characteristics of
657 the slab-mantle wedge interface in transition from its incipient stages into a mature subduction zone.
658 Other intraoceanic arc settings with similar geothermal gradients (e.g. hot subduction zones) may also
659 exhibit similar petrological characteristics.

660 ### 5.3 Insights on the nature of the slab-mantle wedge interface of arcs with intermediate
661 ### *P/T* gradient

662 The slab-mantle wedge interface of a cold mature subduction zone is typically composed of
663 juxtaposed blocks which preserve highly variable peak metamorphic *P-T* conditions, i.e. blueschists
664 and eclogites (Fig. 12a; Guillot et al., 2009). These are attributed to the flow of blocks from different
665 depths along the subduction channel (e.g. Gerya et al., 2002; Guillot et al., 2009). This flow is thought
666 to be enabled by the soft and mechanically weak matrix surrounding the blocks typically dominated
667 by phyllosilicates (e.g. chlorite and serpentine). One notable characteristic of the matrix surrounding
668 the Dalrymple Amphibolite blocks is the predominance of Ca-amphibole and kyanite (e.g. Fig. 8). The
669 strength of these minerals are thought to increase the mechanical strength of the matrix and impede
670 flow of materials along the subduction channel (Penniston-Dorland et al., 2018). Considering that the

671 weaker matrix started forming before the complex reached peak metamorphic conditions, the
672 relatively narrow range of peak *P-T* conditions preserved in the blocks (~600–720 °C; 10–13 kbar)
673 supports this limited flow and the viscous nature of this matrix. Thermodynamic modelling also
674 predicts the prevalence of Ca-amphibole over weaker minerals (e.g. chlorite) in the Stage 2 matrix
675 beyond ~550 °C (Fig. 10c).

676 Processes that lead to the hybrid composition of the matrix in slab-mantle wedge interface
677 mélanges subsequently control the chemistry of arc magmas (e.g. Marschall and Schumacher, 2012).
678 Although the petrogenesis of the matrix in the Dalrymple Amphibolite is investigated in more detail
679 using whole-rock data in Part 2, the chemistry of constituent minerals already provides insights into
680 processes that are possibly at work in this slab-mantle wedge interface. Rutile, a sink for trace elements
681 in the subducting slab, can be used to distinguish the mafic (Cr-rich) and pelitic (Nb-rich) character of
682 a metamorphic rock's protolith (e.g. Meinhold et al., 2008). Rutile in the metamafic blocks from
683 Dalrymple generally fall in the metamafic field (Fig. 6m) while the very high Nb content of those in
684 the Ep-Bt-Ms schist block sample 215-7 fall well into the metapelite field (Fig. 6n). The metamafic
685 block B214-21 from Botoon exhibits interesting Nb content variability tied to its mode of occurrence.
686 Rutile grains in the garnet core have low Nb content (Rt1a = 175–266 ppm) and fall into the metamafic
687 field (Fig. 6). In contrast, those included in garnet mantle and rim and rutile grains in the matrix and
688 included in Camp (Rt1b) have significantly higher Nb content and falls in the metapelite field along
689 with the matrix2a samples (Fig. 6n, B214-2G and B214-14).

690 Nb and Cr contents of rutile do not show any correlation with increasing Zr concentration (i.e.
691 increasing *T*). We interpret the variations in the Nb-Cr contents of rutile in the blocks and matrix (Fig.
692 6m, n) as reflective of the mixing (in a broad sense) of crustal components, i.e. mafic basalts and
693 sediments, during the development of this mélange complex. More detailed investigation of the
694 geochemical characteristics of the matrix is needed to discriminate between the processes which may
695 have controlled its bulk composition, i.e. mechanical mixing, fluid/melt induced advective mixing and
696 diffusion (Marschall and Schumacher, 2012). We therefore only argue that the Nb-Cr variations in the
697 rutile grains indicate the variable involvement of the mafic basalt and sedimentary components. More

importantly, the chemical change in rutile inclusions at the garnet mantle and rim with respect to those at the garnet core suggests that such processes started prior to the blocks reaching peak metamorphic conditions (Fig. 6m). This is consistent with the *P-T-D* history of the surrounding matrix 2a outlined in the previous section.

The involvement of mantle-derived components during this mixing process is less apparent in the Dalrymple Amphibolite. The high *T* condition maintained during the deformation history of the block-in-matrix complex is beyond the serpentine-stability field (Fig. 12a) and the scarce fluid supply at greater depths during incipient subduction due to early devolatilization at shallower regions (e.g. Agard et al., 2018) likely prevented the formation of serpentine. Orthoamphibole-rich blocks in Botoon and the chemical characteristics of some constituent minerals in the matrix2a sample B214-29 however suggest the involvement of mantle components. Kyanite (Cr_2O_3 = 0.71–2.17 wt.%) in B214-29 are relatively Cr-rich while Ca-amphibole grains are both Mg- and Cr-rich (Mg# = 0.72–0.78; Cr_2O_3 = 0.12–1.3 wt.%). Some rutile grains N215-3 also has high Cr_2O_3 content (= 0.16–1.93 wt.%).

The presence of fluids in this shear zone throughout its history is also apparent from the multiple generation of veins cross-cutting the block-in-matrix complex. The earlier stage fluids appear to be in equilibrium with the blocks (i.e. internally sourced; cf. Locatelli et al., 2019) as suggested by the absence of any reaction zone between the vein and the block (e.g. Qz-Ky vein, Figs. 2h, 5a). Monomineralic epidote veins possibly represent Ca-rich fluids. The Qz-Ky veins in particular are interesting since they suggest either a change in the behavior of some immobile elements like Al in this environment similar to what has been described for orogenic belts (e.g. Alpe Sponda, Central Alps; Beitter et al., 2008), or the extreme leaching of the other components which left behind relatively immobile elements. The latter is apparently favored by the occurrence of ilmenite-kyanite accumulations in some sections of matrix2a in Botoon (B214-10; Fig. 8d).

Evidence for migration of externally-derived fluids is also preserved in the latest stage (Stage 3). Microthermometry of fluid inclusions related to the replacement of kyanite by muscovite reveals

724 the involvement of saline fluids (1.8–6.9 wt.% NaCl equivalent; Fig. 10d). Such aqueous fluids with
725 relatively low salinity dominate the shallow regions (< 80 km) of the subduction zone (e.g. Kawamoto
726 et al., 2013; Manning and Frezzotti, 2020). In D113-1, the quartz vein is linked to the replacement of
727 hornblende by actinolite. Compositional maps and line analysis reveal replacive actinolite with
728 progressively higher Si, Ca and Mg# and lower Al, Na and K towards the vein (Fig. 10f, g). The degree
729 of hornblende replacement by actinolite also increases towards the vein. Farther from the vein,
730 actinolite formation is limited along grain boundaries which maps out the pathway of the percolating
731 fluids (Fig. 10h, i). These greenschist-facies fluids were likely derived from the lower-grade
732 lithologies underthrusted below the ophiolite during its exhumation. These observations in the
733 Dalrymple Amphibolite highlight the importance of fluids in element mobility and material transfer
734 through the slab-mantle wedge interface from initiation to its exhumation. Future studies on the
735 chemical signatures of these different generations of fluids may provide further insights on the nature
736 of fluids and fluid-rock interaction along the slab-mantle wedge interface.

737 **5.4 Tectonic implications on the NPCT**

738 The Late Eocene Palawan Ophiolite exposed in central Palawan is argued to have formed as a
739 back-arc basin hosted within the Cretaceous proto-South China Sea (SCS) Plate (Labis et al., 2020;
740 Dycoco et al., 2021). In the Eocene, rifting in the Southeast Asian margin was initiated and the NPCT
741 started drifting toward the southeast (e.g. Yumul et al., 2003; Cao et al., 2020). The shift from a
742 tensional regime to compressional, forced the initiation of subduction at/or near the spreading center
743 of this Eocene proto-SCS (Fig. 12b; Keenan et al., 2016). This convergence resulted in an intraoceanic
744 arc. Slivers of this arc were then emplaced during its collision with the NPCT as the Palawan Ophiolite.

745 The degree to which subduction proceeded in this intraoceanic arc before the underplating of
746 the NPCT and subsequently the emplacement of the ophiolite is largely unknown. The volcanic section
747 of the ophiolite only records its mid-oceanic ridge history (e.g. Keenan et al., 2016; Gibaga et al.,
748 2020) and products of arc magmatism is undetected. Earlier models linked a small volume of calc-
749 alkaline lavas (~17 Ma) in the Cagayan de Sulu ridge to the Eocene subduction initiation (Encarnacion
750 et al., 1995) but the connection remain contentious (e.g. Dycoco et al., 2021).

751 The *P-T-D* evolution of the Dalrymple Amphibolite outlined here however, suggests that
752 subduction along this plate interface did progress, enough to shift its *P-T* gradients towards cooler
753 conditions (Fig. 12a; cf. Agard et al., 2020). Based on the compilation study of Agard et al. (2018),
754 such conditions (~16 °C/km) are usually reached around 2–5 Myr since subduction is initiated (Fig.
755 12b). In contrast, the hot thermal gradients of metamorphic soles are thought to dominate the first ~2
756 Ma since subduction is first initiated. Radiometric dating of the peak metamorphism of the metamafic
757 blocks and the surrounding matrix in the future can further constrain the duration of subduction in the
758 Palawan Ophiolite. Exhumation of the ophiolite with the Dalrymple amphibolite at its base is linked
759 with the complete consumption of the oceanic lithosphere at the leading edge of the NPCT and
760 continental material underplating beneath the arc.

761 **6. Conclusions**

762 The *P-T-D* history of the Dalrymple Amphibolite underlying the Palawan Ophiolite are discussed
763 in Part 1 of this thesis. The prograde *P-T* path preserved in the metamafic blocks indicate cooler
764 paleogeothermal gradients (~16 °C/km) compared to typical metamorphic soles (>20 °C/km). The
765 peak *P-T* conditions of the metamafic blocks, i.e. amphibolites, Ep amphibolites and Grt amphibolites,
766 and the surrounding matrix are also shown to be similar (~700 °C, 13 kbar). The block-in-matrix
767 structure of the Dalrymple Amphibolite indicates that this complex likely represents the slab-mantle
768 wedge interface of a subduction zone already in its infancy. Field characteristics, matrix2a *P-T*
769 conditions and Cr and Nb contents of rutile grains indicate that the matrix-forming deformation likely
770 started prior to the rock sequence reaching peak metamorphic conditions at depths of approximately
771 ~45 km. Deformation events accompanying each metamorphic stage also affected the textural and
772 petrological characteristics of this block-in-matrix sequence. Multiple generation of veins and lenses
773 of veins cross-cutting the block-in-matrix sequence reveal the important role of fluids in material
774 transfer along the slab-mantle wedge interface throughout its history. The petrological characteristics
775 and *P-T-D* history of the Dalrymple Amphibolite therefore provide important insights on the nature
776 of the slab-mantle wedge interface of an arc with intermediate *P/T* geothermal gradients which is
777 prevalent during incipient subduction and in warm subduction complexes.

778 **ACKNOWLEDGEMENTS**

779 We acknowledge the logistical support provided by the Rushurgent Working Group of the University
780 of the Philippines Diliman, the Palawan Council for Sustainable Development (PCSD) and the local
781 government units (LGUs) of Puerto Princesa, Palawan (SEP Clearance UAC-011519-024) during our
782 fieldwork. M. Takaya of Kyoto University is thanked for the preparation of thin sections. Valuable
783 discussions with T. Hirajima and K. Naemura are also appreciated. This work forms part of the
784 doctoral thesis of the first author under the Japanese Government (Monbukagakusho) scholarship
785 program. This work was supported by the JSPS KAKENHI Grant Number JP19H01991 of the second
786 author and a research grant from the National Research Council of the Philippines (NRCP P-028) of
787 the third author. Comments from an anonymous reviewer and T. Lamont helped improve the initial
788 version of this manuscript. Editorial handling by Prof. R. White is also highly appreciated.

789

790 **References**

791 Agard, P., Prigent, C., Soret, M., Dubacq, B., Guillot, S., Deldicque, D., 2020. Slabitization:
792 mechanism controlling subduction development and viscous coupling. Earth-Science Reviews
793 28, 1–28.

794 Agard, P., Plunder, A., Angiboust, S., Bonnet, G., Ruh, J., 2018. The subduction plate interface: rock
795 record and mechanical coupling (from long to short timescales). Lithos 320–321, 537–566.

796 Agard, P., Yamato, P., Soret, M., Pringent, C., Guillot, S., Plunder, A., Dubacq, B., Chauvet, A.,
797 Monie, P., 2016. Plate interface rheological switches during subduction infancy: Control on
798 slab penetration and metamorphic sole formation. Earth and Planetary Science Letters 451,
799 208–220.

800 Angel, R.J., Mazzuccheli, M.L., Alvaro, M., Nestola, F., 2017a. EoSFit-Pinc: A simple GUI for host-
801 inclusion elastic thermobarometry. American Mineralogist 102, 1957–1960.

802 Angel, R.J., Alvaro, M., Miletich, R., Nestola, F., 2017b. A simple and generalized *P-T-V* EoS for
803 continuous phase transitions, implemented in EosFit and applied to quartz. Contributions to
804 Mineralogy and Petrology 29, 1–15.

Aurelio, M.A., Forbes, M., Taguibao, K.J.L., Savella, R., Bacud, J., Franke, D., Pubellier, M., Savva, D., Meresse, F., Steuer, S., Carranza, C.D., 2014. Middle to Late Cenozoic tectonic events in south and central Palawan (Philippines) and their implications to the evolution of the southeastern margin of South China Sea: Evidence from onshore structural and offshore seismic data. Marine and Petroleum Geology 58, 658–673.

Bebout, G.E., 2013. Metasomatism in subduction zones of subduction zones of subducted oceanic slabs, mantle wedges, and the slab-mantle interface *In*: Harlov, D.E., Austrheim, H. Metasomatism (eds.) Metasomatism and the chemical transformation of rock. Lecture notes in Earth system sciences, Springer-Verlag Berlin Heidelberg, 289–349.

Bebout, G.E., Barton, M.D., 2002. Tectonic and metasomatic mixing in a High-*T*, subduction-zone melange – insights into the geochemical evolution of the slab-mantle interface. Chemical Geology 187, 79–106.

Bebout, G.E., Penniston-Dorland, S.C., 2016. Fluid and mass transfer at subduction interfaces-The field metamorphic record. Lithos 240–243, 228–258.

Beitter, T., Wagner, T., Marki, G., 2008. Formation of kyanite-quartz veins of the Alpe Sponda, Central Alps, Switzerland: Implications for Al transport during regional metamorphism. Contributions to Mineralogy and Petrology 156, 689–707.

Bodnar, R.J., 1993. Revised equation and table for determining the freezing point depression of H_2O-NaCl solutions. Geochimica et Cosmochimica Acta 57, 683–684.

Cao, L., Shao, L., Qiao, P., Cui, Y., Zhang, G., Zhang, X., 2020. Formation and paleogeographic evolution of the Palawan continental terrane along the Southeast Asian margin revealed by detrital fingerprints. The Geological Society of America Bulletin 133, 1167–1193.

Codillo, E.A., Le Roux, V., Marschall, H.R., 2018. Arc-like magmas generated by melange-peridotite interaction in the mantle wedge. Nature Communications 9, 1–11.

Cowan, R.J., Searle, M.P., Waters, D.J., 2014. Structure of the metamorphic sole to the Oman Ophiolite, Sumeini Window and Wadi Tayyin; Implications for ophiolite obduction processes. Geological Society, London, Special Publications 392, 155–175.

De Capitani, C., Brown, T.H., 1987. The computation of chemical equilibrium in complex systems containing non-ideal solutions. Geochimica et Cosmochimica Acta 51, 2639–2652.

De Capitani, C., Petrakakis, K., 2010. The computation of equilibrium assemblage diagrams with Theriak/Domino software. American Mineralogist 95, 1006–1016.

836 Dilek, Y., Furnes, H., 2014. Ophiolites and their origins. Elements 10, 93–100.

837 Dycoco, J.M.A., Payot, B.D., Valera, G.T.V., Labis, F.A.C., Pasco, J.A., Perez, A.d.C., Tani, K., 2021.
838 Juxtaposition of Cenozoic and Mesozoic ophiolites in Palawan island, Philippines: New
839 insights on the evolution of the Proto-South China Sea. Tectonophysics 819. 229085.

840 Droop, G.T.R., 1987. A general equation for estimating Fe^{3+} concentrations in ferromagnesian
841 silicates and oxides from microprobe analyses, using stoichiometric criteria. Mineralogical
842 Magazine 51, 431–435.

843 Encarnacion, J.P., Essene, E.J., Mukasa, S.B., Hall, C.H., 1995. High-pressure and -temperature
844 subophiolitic kyanite-garnet amphibolites generated during initiation of Mid-Tertiary
845 subduction, Palawan, Philippines. Journal of Petrology 36, 1481–1503.

846 Garcia-Casco, A., Lazaro, C., Rojas-Agramonte, Y., Kröner, A., Res-Roldan, R.L.T., Nuñez, K.,
847 Neubauer, F., Millan, G., Blanco-Quintero, I., 2008. Partial melting and counterclockwise *P-T*
848 path of subducted oceanic crust (Sierra del Colvento Mélange, Cuba). Journal of Petrology 49,
849 129–161.

850 Gerya T., Stöckhert, B., Perchuk, A.L., 2002. Exhumation of high-presure metamorphic rocks in a
851 subduction channel: A numerical simulation. Tectonics 21, 1–15.

852 Gibaga, C.R.L., Arcilla, C.A., Hoang, N., 2020. Volcanic rocks from the Central and Southern
853 Palawan Ophiolites, Philippines: Tectonic and mantle heterogeneity constraints. Journal of
854 Asian Earth Sciences: X, 1–17. DOI: 10.1016/j.jaesx.2020.100038.

855 Gilgen, S., Diamond, L.W., Mercolli, I., 2016. Sub-seafloor epidosite alteration: Timing, depth and
856 stratigraphic distribution in the Semail Ophiolite, Oman. Lithos 260, 191–210.

857 Green, E.C.R., White, R.W., Diener, J.F.A., Powell, R., Holland, T.J.B., Palin, R.M., 2016. Activity-
858 composition relations for the calculation of partial melting equilibria in metabasic rocks.
859 Journal of Metamorphic Geology 34, 845–869.

860 Grove, M., Bebout, G.E., 1995. Cretaceous tectonic evolution of coastal southern California: Insights
861 from the Catalina Schist, Tectonics 14, 1290–1308.

862 Guillot, S., Hattori, K., Agard, P., Schwartz, S., Vidal, O., 2009. Exhumation processes in oceanic and
863 continental subduction contexts: A review *In*: Lallemand, S., Funiciello, F. (eds.) Subduction
864 zone geodynamics. Springer-Verlag Berlin Heidelberg, 175–205.

865 Hacker, B.R., 1990. Simulation of the metamorphic and deformational history of the metamorphic
866 sole of the Oman ophiolite. Journal of Geophysical Research 95, 4895–4907.

867 Holland, T.J.B., Powell, R., 2011. An improved and extended internally consistent thermodynamic
868 dataset for phases of petrological interest, involving a new equation of state for solids. Journal
869 of Metamorphic Geology 29, 333–383.

870 Jagoutz, O., Behn, M.D., 2013. Foundering of lower island-arc crust as an explanation for the origin
871 of the continental Moho. Nature 504, 131–134.

872 Jørgensen, T.R.C., Tinkham, D.K., Lesher, C.M., 2019. Low-*P* and high-*T* metamorphism of basalts:
873 Insights from the Sudbury impact melt sheet aureole and thermodynamic modelling. Journal of
874 Metamorphic Geology 37, 271–313.

875 Kapp, P., Manning, C.E., Tropper, P., 2009. Phase-equilibrium constraints on titanite and rutile
876 activities in mafic epidote amphibolites and geobarometry using titanite-rutile equilibria.
877 Journal of Metamorphic Geology 27, 509–521.

878 Kawamoto, T., Yoshikawa, M., Kumagai, Y., Mirabueno, H.T., Okuno, M., Kobayashi, T., 2013.
879 Mantle wedge infiltrated with saline fluids from dehydration and decarbonation of subducting
880 slab. Proceedings of the National Academy of Sciences 110, 9663–9668.

881 Keenan, T.E., Encarnacion, J., Buchwaldt, R., Fernandez, D., Mattinson, J., Rasoazanamparany, C.,
882 Leutkemeyer, P.B., 2016. Rapid conversion of an oceanic spreading center to a subduction zone
883 inferred from high-precision geochronology. Proceedings of the National Academy of Sciences
884 113, E7359–E7366.

885 Kohn, M.J., Spear, F.S., 1990. Two new geobarometers for garnet amphibolites, with applications to
886 southeastern Vermont. American Mineralogist 75, 89–96.

887 Labis, F.A.C., Payot, B.D., Valera, G.T.V., Pasco, J.A., Dycoco, J.M.A., Tamura, A., Morishita, T.,
888 Arai, S., 2020. Melt-rock interaction in the subarc mantle: records from the plagioclase
889 peridotites of the southern Palawan Ophiolite, Philippines. International Geology Review 63,
890 1067–1089.

891 Lamont, T.N., Roberts, N.M.W., Searle, M.P., Gopon, P., Waters, D.J., Millar, I., 2020. The age,
892 origin and emplacement of the Tsiknias Ophiolite, Tinos, Greece, Tectonics, 39, 1–45.

893 Leake, B.E., Woolley, A.R., Arps, C.E.S., Birch, W.D., Gilbert, M.C., Grice, J.D., Hawthorne, F.C.,
894 Kato, A., Kisch, H.J., Krivovichev, V., Linthout, K., Laird, J., Mandarino, J.A., Maresch, W.V.,
895 Nickel, E.H., Rock, N.M.S., Schumacher, J.C., Smith, D.C., Stephenson, N.C.N., Ungaretti, L.,
896 Whittaker, E.J.W., Youzhi, G., 1997. Nomenclature of amphiboles: Report of the subcommittee
897 on amphiboles of the international mineralogical association, commission on new minerals and
898 mineral names. The Canadian Mineralogist 35, 219–246.

899 Locatelli, M., Verlaguet, A., Agard, P., Pettke, T., Federico, L., 2019. Fluid pulses during stepwise
900 brecciation at intermediate subduction depths (Monviso Eclogites, W. Alps): First internally
901 then externally sourced. Geochemistry, Geophysics, Geosystems 20, 5285–5318.

902 Manning, C.E., Frezzotti, M.L., 2020. Subduction-zone fluids. Elements 16, 395–400.

903 Marschall, H.R., Schumacher, J.C., 2012. Arc magmas sourced from melange diapirs in subduction
904 zones. Nature Geoscience 5, 862–867.

905 Meinhold, G., Anders, B., Kostopoulos, D., Reischmann, T., 2008. Rutile chemistry and thermometry
906 as provenance indicator: An example from Chios Island, Greece. Sedimentary Geology 203,
907 98–111.

908 Muller, C., 1991. Biostratigraphy and geological evolution of the Sulu sea and surrounding area. *In*:
909 Silver, E.A., Rangin, C., von Breymann, M.T. et al. Proceedings of the Ocean Drilling Program
910 Scientific Results 124, College Station, Texas, 121–131.

911 Padrones, J.T., Tani, K., Tsutsumi, Y., Imai, A., 2017. Imprints of Late Mesozoic tectono-magmatic
912 events on Palawan Continental Block in northern Palawan, Philippines. Journal of Asian Earth
913 Sciences 142, 56–76.

914 Peacock, S., Wang, K., 1999. Seismic consequences of warm versus cool subduction metamorphism:
915 Examples from Southwest and Northeast Japan. Science 286, 937–939.

916 Penniston-Dorland, S.C., Kohn, M.J., Piccoli, P.M., 2018. A melange of subduction temperatures:
917 Evidence from Zr-in-rutile thermometry for strengthening of the subduction interface. Earth
918 and Planetary Science Letters 482, 525–535.

919 Picazo, S.N., Ewing, T.A., Müntener, O., 2019. Paleocene metamorphism along the Pennine-
920 Austroalpine suture constrained by U-Pb dating of titanite and rutile (Malenco, Alps). Swiss
921 Journal of Geosciences 112, 517–542.

922 Rangin, C., Silver, E.A., 1991. Neogene tectonic evolution of the Celebes-Sulu basins: New insights
923 from Leg 124 Drilling. Proceedings of the Ocean Drilling Program. Scientific Results 124, 51–
924 63.

925 Raschka, H., Nacario, E., Rammlair, D., Samonte, C., Steiner, L., 1985. Geology of the ophiolite of
926 central Palawan island, Philippines. Ofioliti 10, 375–390.

927 Rioux, M., Garber, J., Bauer, A., Bowring, S., Searle, M., Kelemen, P., Hacker, B., 2016. Synchronous
928 formation of the metamorphic sole and igneous crust of the Semail ophiolite: New constraints
929 on the tectonic evolution during ophiolite formation from high-precision U-Pb zircon
930 geochronology. Earth and Planetary Science Letters 451, 185–195.

931 Schmidt, C., Ziemann, M.A., 2000. In-situ Raman spectroscopy of quartz: A pressure sensor for
932 hydrothermal diamond-anvil cell experiments at elevated temperatures. American Mineralogist
933 85, 1725–1734.

934 Schumacher, J.C., 1991. Empirical ferric iron corrections: necessity, assumptions and effects on
935 selected geothermobarometers. Mineralogical Magazine 55, 3–18.

936 Seyfried, W.E., Berndt, M.E., Seewald, J.S., 1988. Hydrothermal alteration processes at mid-ocean
937 ridges: Constraints from diabase alteration experiments, hot-spring fluids and composition of
938 the oceanic crust. Canadian Mineralogist 26, 787–804.

939 Soret, M., Agard, P., Dubacq, B., Plunder, A., Yamato, P., 2017. Petrological evidence for stepwise
940 accretion of metamorphic soles during subduction infancy (Semail ophiolite, Oman and UAE).
941 Journal of Metamorphic Geology 35, 1051–1080.

942 Starr, P.G., Pattison, D.R.M., 2019. Metamorphic devolatilization of basalts across the greenschist-
943 amphibolite facies transition zone: Insights from isograd mapping, petrography and
944 thermodynamic modelling. Lithos 342–343, 295–314.

945 Steele-MacInnis, M., Lecumberri-Sanchez, P., Bodnar, R.J., 2012. HOKIEFLINCS_H2O-NACL: A
946 Microsoft Excel spreadsheet for interpreting microthermometric data from fluid inclusions
947 based on the PVTX properties of H_2O-NaCl. Computers & Geosciences 49, 334–337.

948 Suzuki, K., Kawakami, T., 2019. Metamorphic pressure-temperature conditions of the Lützow-Holm
949 Complex of East Antarctica deduced from Zr-in-rutile geothermometer and Al_2SiO_5 minerals
950 enclosed in garnet. Journal of Mineralogical and Petrological Sciences 114, 267–279.

951 Thomas, J.B., Spear, F.S., 2018. Experimental study of quartz inclusions in garnet at pressures up to
952 3.0 GPa: evaluating validity of the quartz-in-garnet inclusion elastic thermobarometer.
953 Contributions to Mineralogy and Petrology 42, 1–14.

954 Tomkins, H. S., Powell, R., Ellis, D. J., 2007. The pressure dependence of the zirconium-in-rutile
955 thermometer. Journal of Metamorphic Geology 25, 703–713.

956 Ulmer, P., Trommsdorff, V., 1995. Serpentine stability to mantle depths and subduction-related
957 magmatism. Science 268, 858–861.

van Hinsbergen, D.J.J, Peters, K., Maffione, M., Spakman, W., Guilmette, C., Thieulot, C., Plümper, O., Gürer, D., Brouwer, F.M., Aldanmaz, E., Kaymackci, N., 2015. Dynamics of intraoceanic subduction initiation: 2. Suprasubduction zone ophiolite formation and metamorphic sole exhumation in context of absolute plate motions. Geochemistry, Geophysics, Geosystems 16, 1771–1785.

Vielzeuf, D., Schmidt, M.W., 2001. Melting relations in hydrous systems revisited: Application to metapelites, metagreywackes and metabasalts. Contributions to Mineralogy and Petrology 141, 251–267.

Wakabayashi, J., 2017. Structural context and variation of ocean plate stratigraphy, Franciscan Complex, California: Insight into mélange origins and subduction-accretion processes. Progress in Earth and Planetary Science 4, 1–23.

Wei, C.J., Duan, Z.Z., 2018. Phase relations in metabasic rocks: Constraints from the results of experiments, phase modelling and ACF analysis. *In*: Zhang, L.F., Zhang, Z., Schertl, H.-P., Wei, C. (eds.) HP-UHP Metamorphism and tectonic evolution of orogenic belts. Geological Society, London, Special Publications 474, 1–21.

Whitney, D.L., Evans, B.W., 2010. Abbreviations for names of rock-forming minerals. American Mineralogist 95, 185–187.

Yumul, G.P.Jr., Dimalanta, C.B., Tamayo, R.A.Jr., Maury, R.C., 2003. Collision, subduction and accretion events in the Philippines: A synthesis. The Island Arc 12, 77–91.

Zack, T., Moraes, R., Kronz, A., 2004. Temperature dependence of Zr in rutile: Empirical calibration of a rutile thermometer. Contributions to Mineralogy and Petrology 148, 471–488.

979

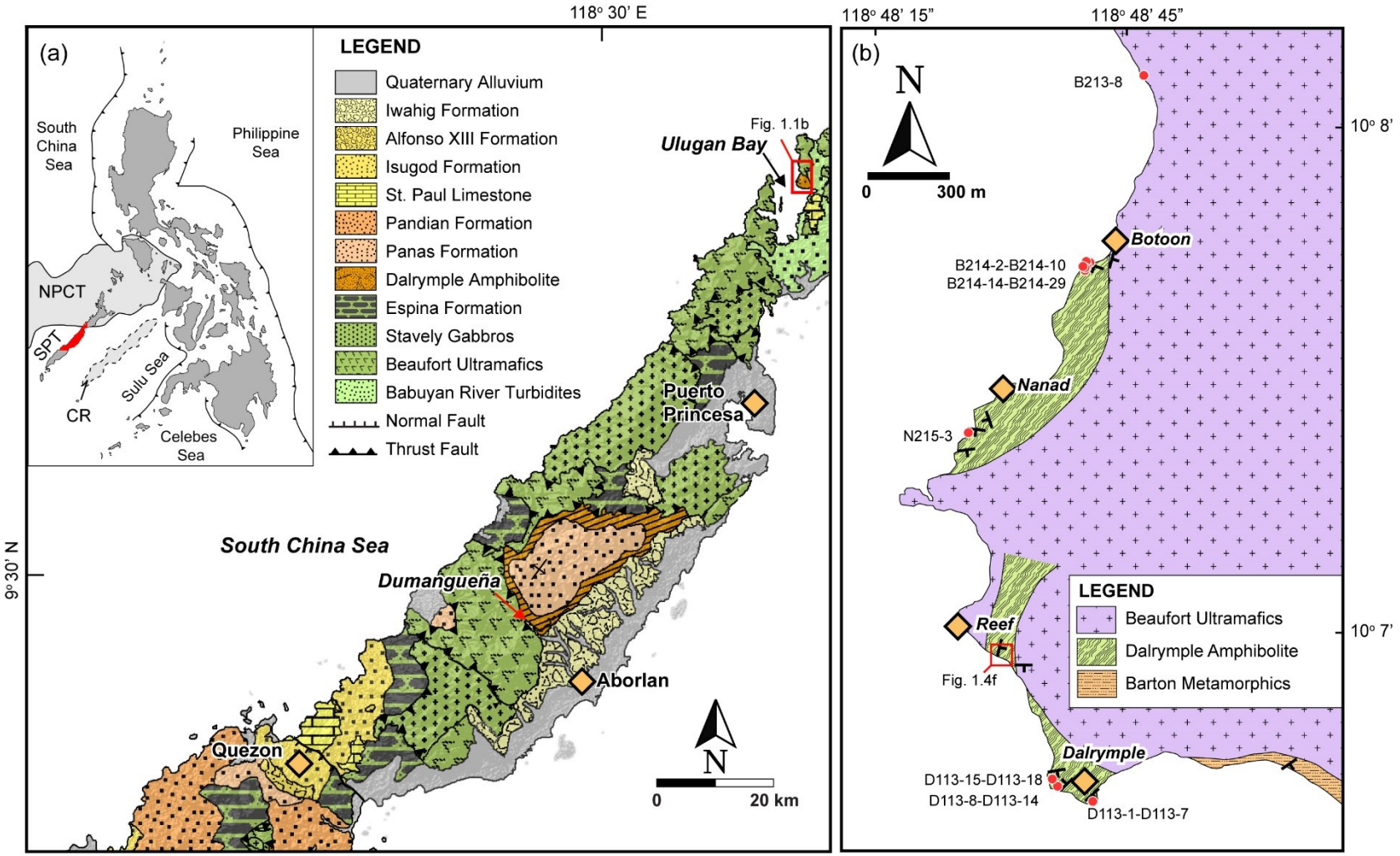

Fig. 1. a) Map showing the distribution of lithologies in central Palawan. The metamorphic sole is exposed in Ulugan Bay, Puerto Princesa and Dumangueña, Aborlan. Inset map shows tectonic map of the Philippines, the surrounding marginal basins and trenches. NPCT-North Palawan Continental Terrane, SPT-South Palawan Terrane, CR-Cagayan de Sulu Ridge. Modified from Labis et al. (2020); b) Distribution of Dalrymple Amphibolite and sampling points in Ulugan Bay modified from Encarnacion et al. (1995). The localities discussed in the text are marked as diamonds.

980

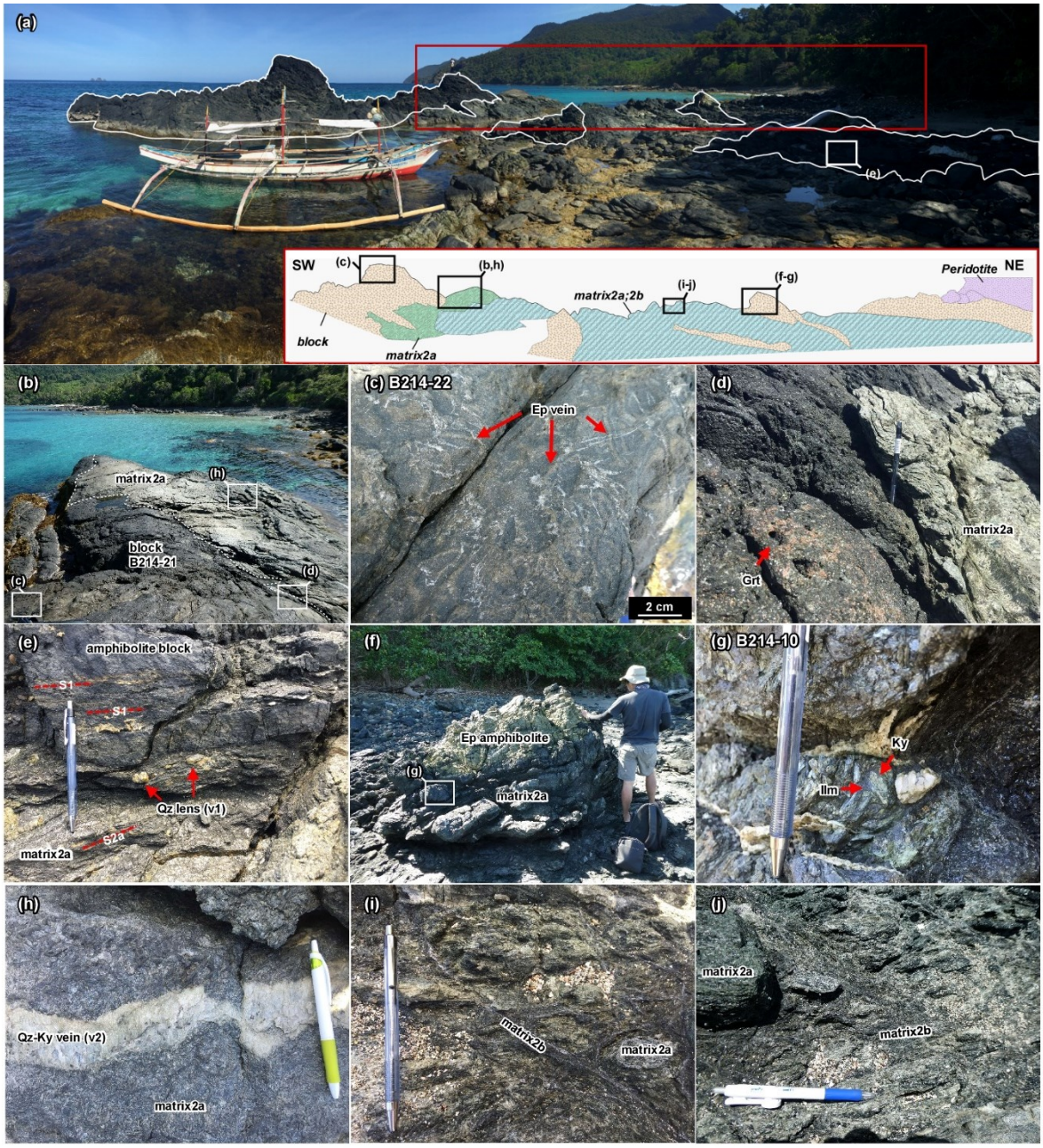

Fig. 2. Field photos of the exposure in Botoon point. a) Panoramic photo of the block and matrix sequence. Inset shows a schematic representation of the area enclosed in red box showing the blocks (white solid lines) and the matrix in the low lying portions of the exposure. b–d) Melanocratic metamafic block surrounded by lighter matrix2a and cut by epidote veins. e) Foliation (S1) parallel quartz lenses. f) Matrix2a below the Ep amphibolite block which shows g) Coarse kyanite crystals surrounded by ilmenite. h) Qz-Ky veins in the surrounding matrix2a. i,j) Matrix2a transected by later matrix2b.

981

982

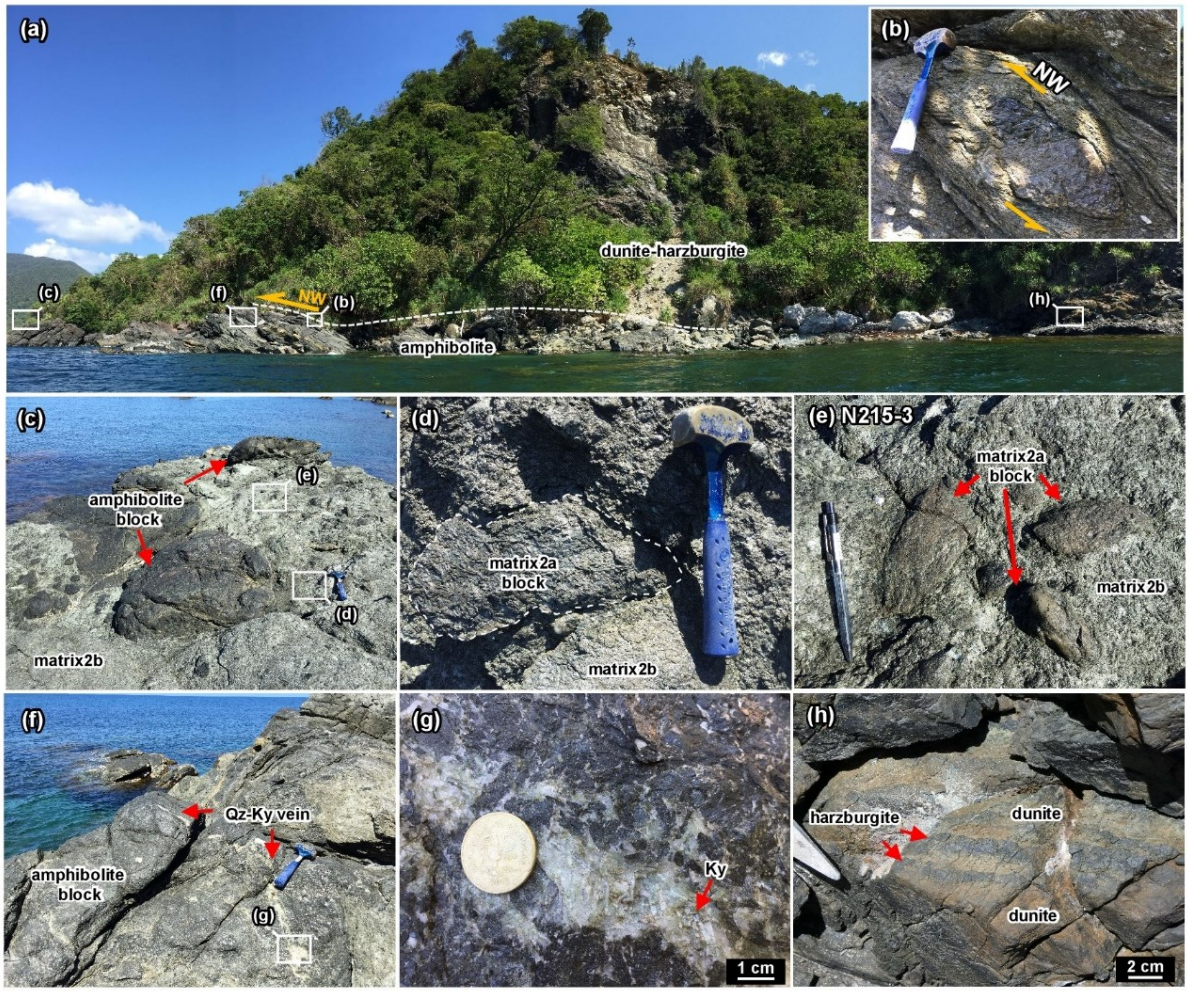

Fig. 3. Field photos of the exposure in Nanad. a) Panoramic photo showing the thrust boundary between the metamorphic sole and the overlying peridotites. b) Shear sense indicator suggests a top to NW movement. c) Rounded metamafic blocks surrounded by the lighter-colored and highly sheared matrix2b. d–e) Matrix2a lenses transformed into small rounded blocks. f, g) Metamafic block transected by Qz-Ky vein which terminates in the surrounding matrix2b. h) Dunite-harzburgite interlayers which comprise the hanging wall in Nanad.

983

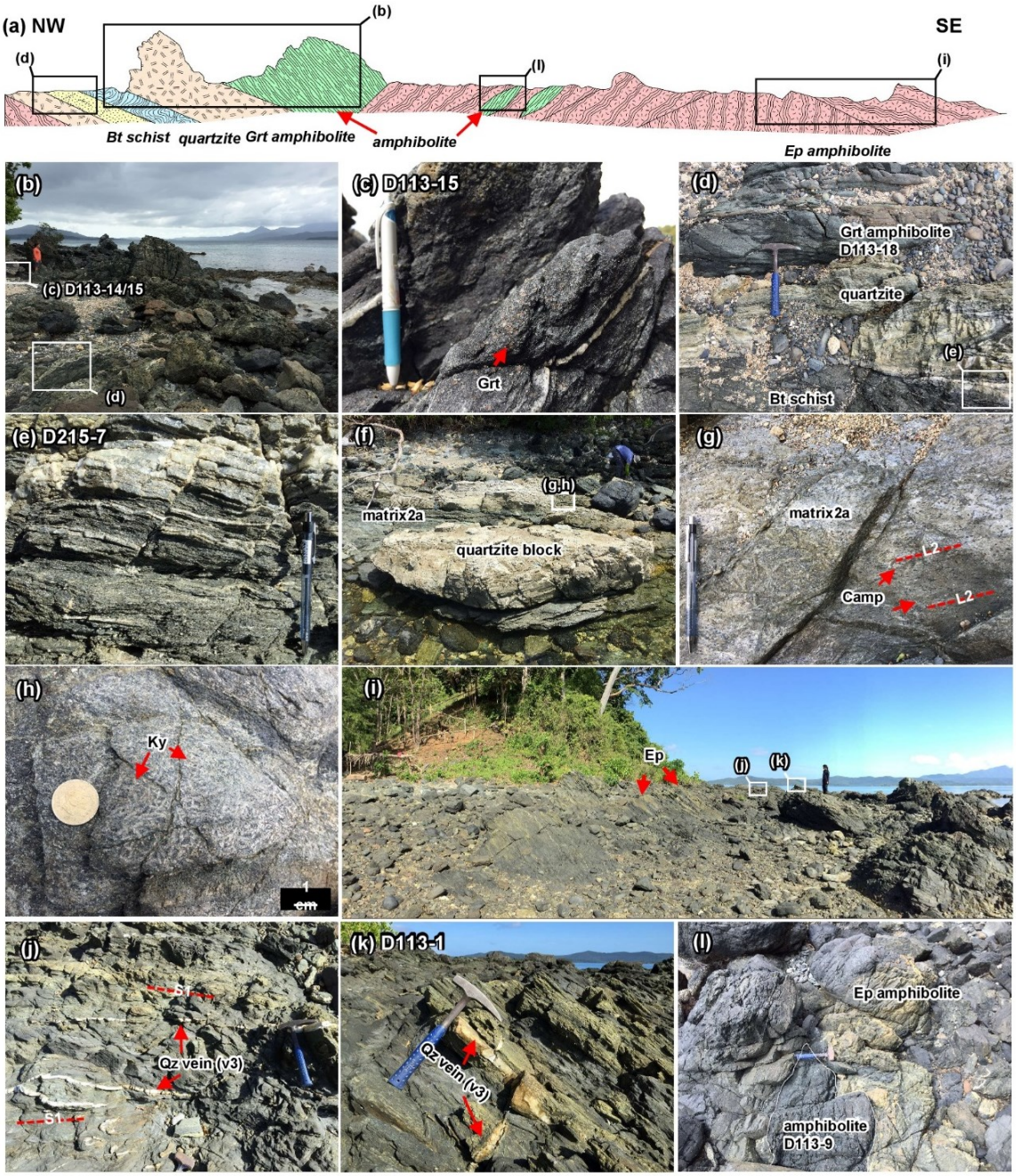

Fig. 4. Field photos in Dalrymple point. a) Schematic representation of the exposure showing the block-dominated NW section and the more coherent Ep amphibolite sequence in the SE side. The boxes indicate the relative position of the field photos. b–e) Interlayers of Grt amphibolite, quartzite and Bt schist blocks. f) Quartzite block surrounded by matrix2a. g–h) Kyanite pseudomorphed by muscovite, and Ca-amphibole in matrix2a. i) Relatively coherent Ep amphibolite block cut by later stage j–k) Quartz veins (v3) which transect the foliation of the blocks (S1). In Fig. 1.4 j, k, epidote-rich domains are the yellowish portions while the darker parts are the epidote-poor domains. l) Amphibolite lens surrounded by Ep amphibolite.

984

985

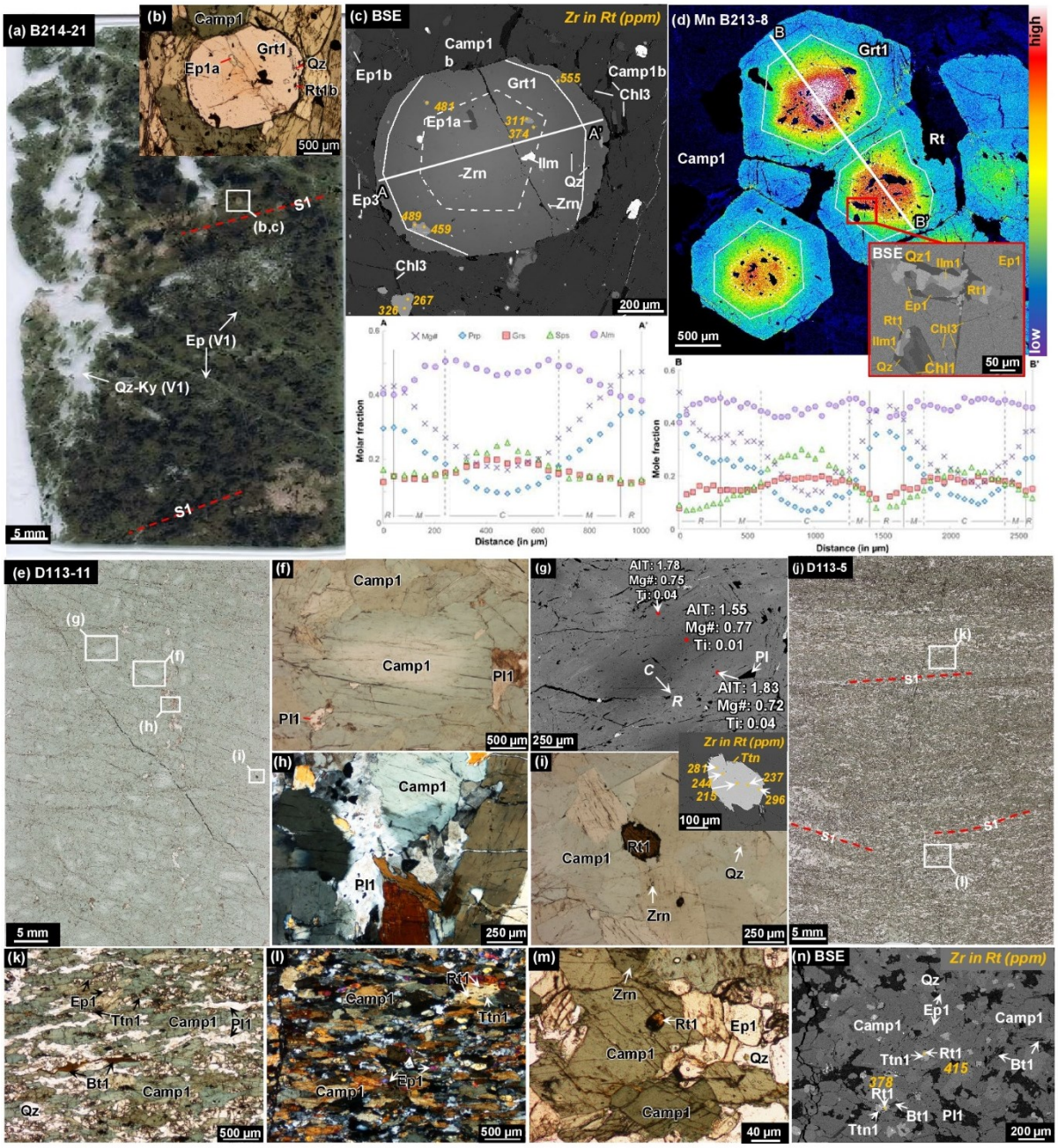

Fig. 5. Photomicrographs, BSE images and X-ray elemental map of the blocks. a) Grt amphibolite block showing foliation direction delineated by the linear arrangement of garnet porphyroblasts and long axis direction of Ca-amphibole. An earlier epidote-vein (V1) is transected by a discordant Qz-Ky vein (V1). Garnet porphyroblasts in plane polarized light (PPL; 1.5b) and back-scattered electron image (BSE; 1.5c) showing inclusion assemblage at the core (C), mantle (M) and rim (R) delineated in the line analysis (A-A'). d) X-ray elemental map showing distribution of Mn in the garnet porphyroblast and the multiphase solid inclusion (MSI) composed of Rt+Ilm+Chl+Qz+Ep+Qz at the garnet core identified by line analysis (B-B'). e) PPL; Amphibolite block composed of f) PPL; Coarse Ca-amphibole with optical zonation. g) BSE image of one Ca-amphibole showing difference in Al_T, Mg# and Ti content of the core (C) compared to the rim (R). h) in cross-polarized light (XPL), plagioclase (Pl1) in the amphibolite blocks are mostly interstitial while i) in PPL; Rutile grains are sometimes partially replaced by titanite. j, k) in PPL; l) in XPL; Epidote amphibolite are fine-grained and composed of foliated Camp+Bt+Pl+Ep+Qz+Ttn. m) in PPL; Rt+Zrn+Qz assemblage included in the Ca-amphibole and n) BSE; In the matrix surrounded by titanite.

986

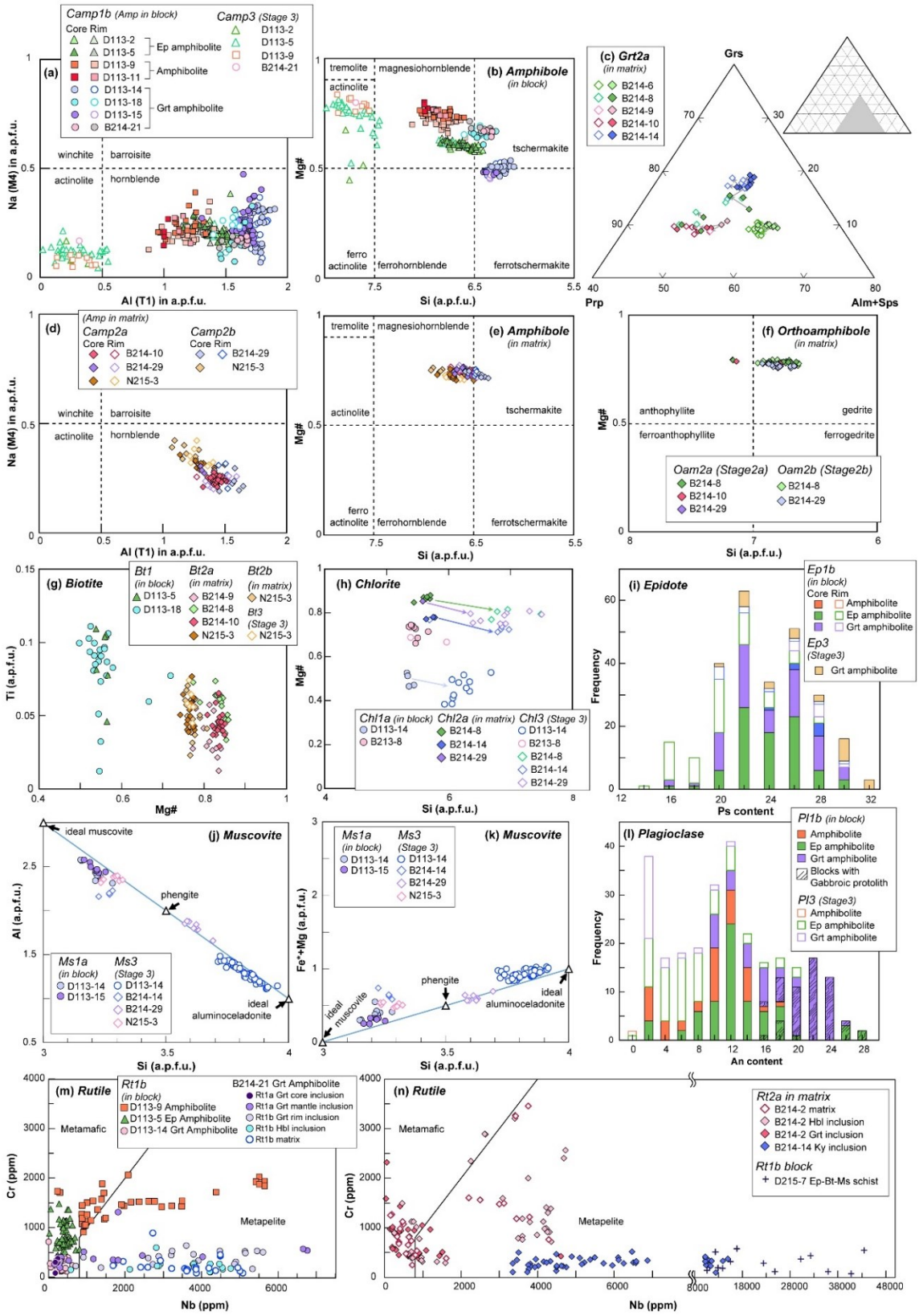

Fig. 6. Mineral chemistry of blocks and matrix from the Dalrymple Amphibolite. Legends are the same for a and b, and d and e. a, b) Amphibole in the blocks. c) Garnet composition and d, e) Amphiboles in the matrix2a samples. f) Point analysis of orthoamphiboles in the matrix and g) Biotite and h) Chlorite in the Ep amphibolite (triangle), Grt amphibolite (circles) blocks and matrix samples. i) Histogram showing pistacite content of epidote in the Dalrymple Amphibolites. j, k) Point analysis of muscovite in the Grt amphibolite blocks compared to Stage 3 alteration. l) Histogram of the anorthite content of plagioclases. m, n) Cr vs Nb concentration of rutile grains in the blocks and the matrix. Note the change in scale in Fig. 1.6 m, n to accommodate the high-Nb rutile grains. The metamafic and metapelite fields are from Meinhold et al. (2008).

987

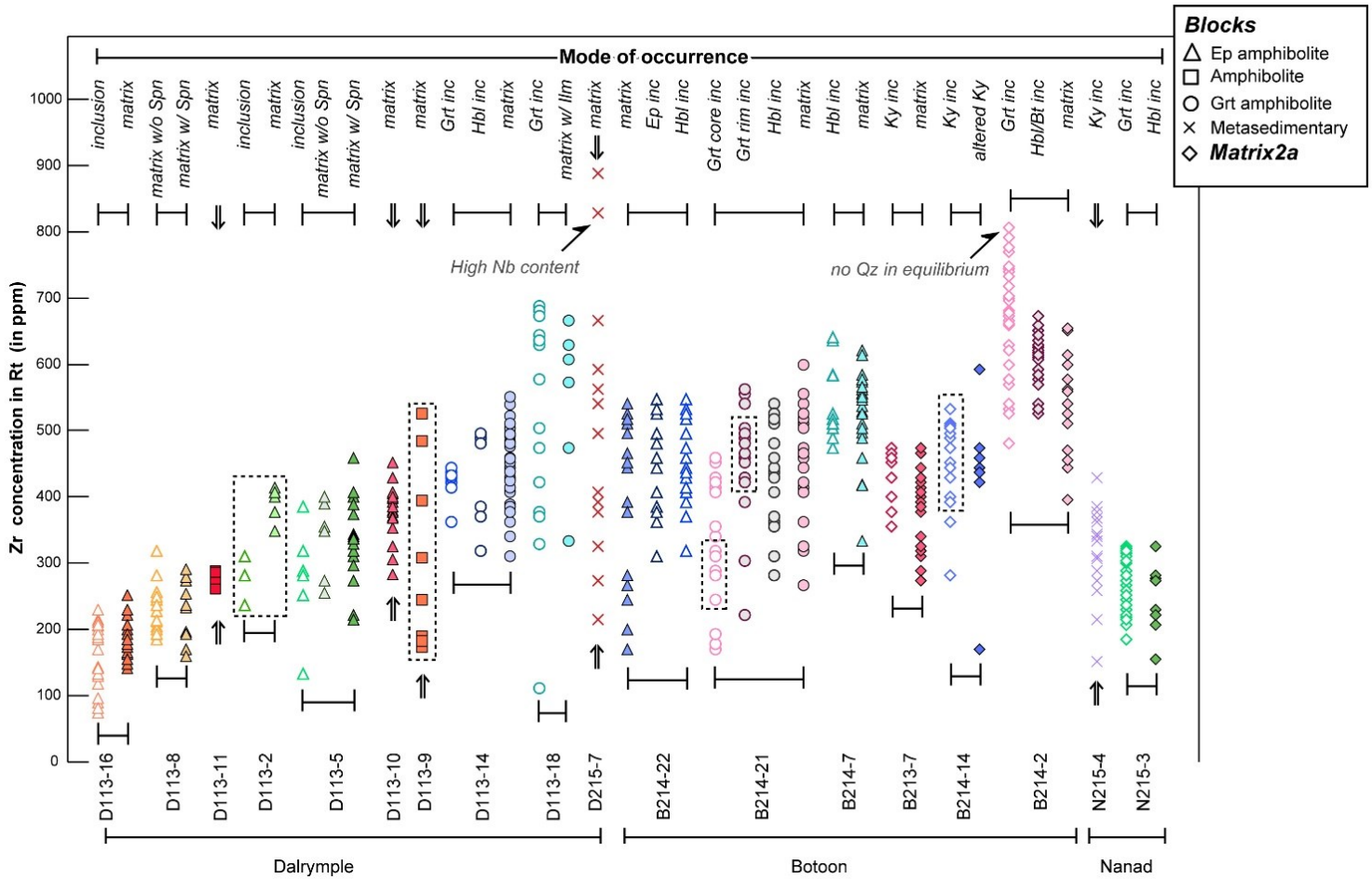

Fig. 7. Zr content of rutile grains in blocks and matrix2a samples of Dalrymple Amphibolite and their modes of occurrence. Several factors may result to lower Zr concentration in rutile which may cause the underestimation of peak *T* conditions. These range from primary processes (e.g. timing of formation relative to *P-T* path) to secondary processes such as retrograde growth and diffusive loss during cooling (Penniston-Dorland et al., 2018). In contrast, conditions such as the absence of quartz in equilibrium with rutile observed in B214-2G garnet inclusions could result to higher Zr concentration in rutile (Tomkins et al., 2007). Penniston-Dorland et al. (2018) suggested the use of "Mean Maximum Zr-in-rutile" along with textural constraints in interpreting and estimating peak metamorphic conditions. This method was adopted in this study in selecting rutile analysis used for geothermometry. The rutile grains used for geothermobarmetry in Fig. 1.9 are bordered by rectangles with dashed borders. The rutile grains in the metasedimentary sample D215-7 have very high Nb content (>17,000 ppm) which may have possibly affected its crystal structure (Zack et al., 2004). The Zr content of these rutile grains were therefore not used to estimate *P-T* conditions.

988

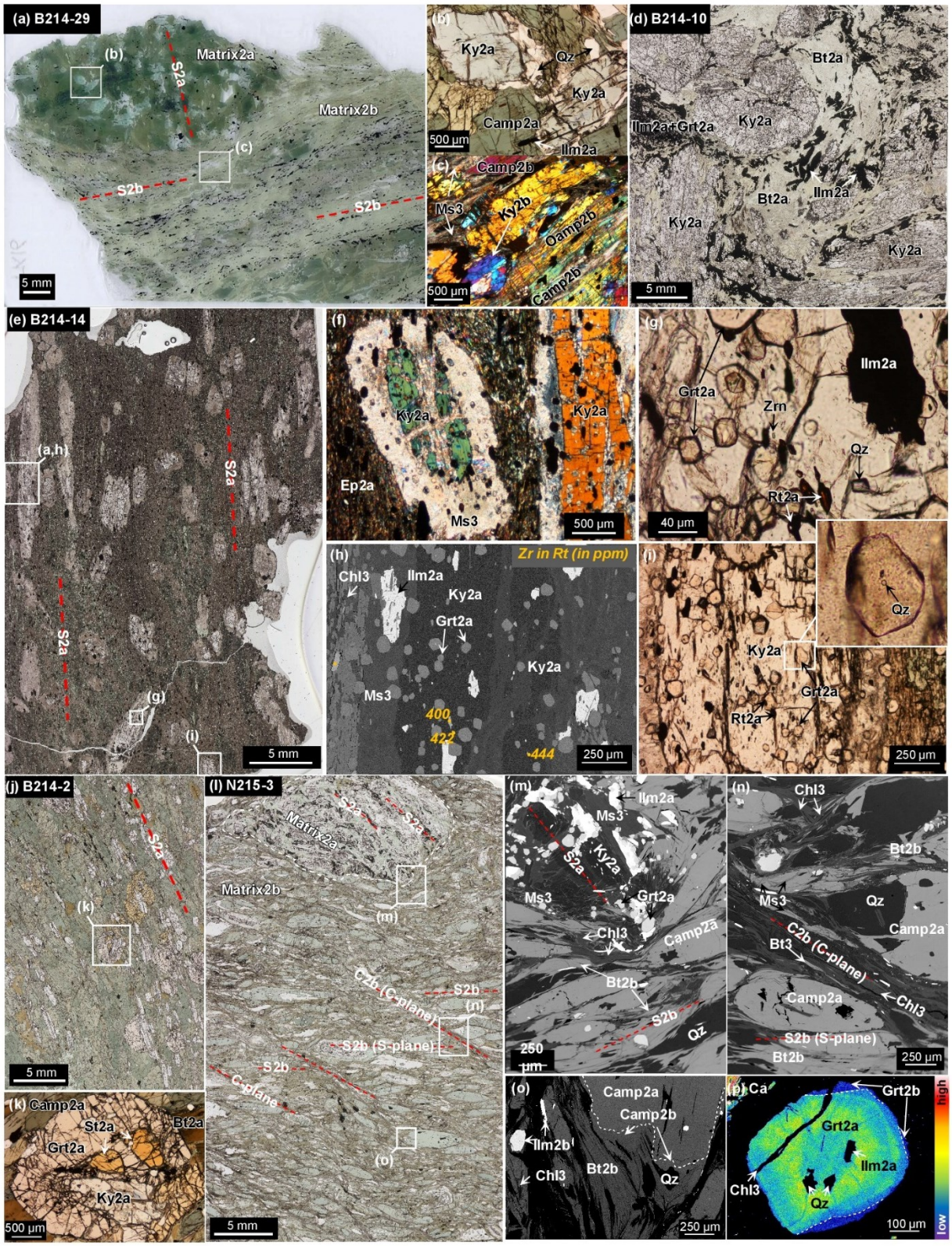

Fig. 8. Photomicrographs (in XPL and PPL) and BSE images of matrix samples. a) in PPL; Matrix2a block with foliation (S2a) surrounded by matrix2b which exhibit a distinct foliation (S2b). b) in PPL; The matrix2a has the same mineralogy as c) Matrix2b (in XPL). d) in PPL; Ilm2a accumulations surrounding coarse Ky2a grains. e, f) in PPL; Matrix2a sample B214-14. g) in PPL; Kyanite porphyroblasts include Zrn-Rt-Qz assemblage used for h) Zr-in-rutile geothermometry (BSE). i) in PPL; Quartz inclusion in garnet (Grt2a) in turn hosted by kyanite used for elastic geobarometry. j, k) in PPL; Grt+St+Bt+Camp+Ky bearing matrix2a. l) in PPL; Matrix2a block surrounded by matrix2b showing crenulations and multiple deformation stages marked by different foliation planes. m, n) BSE images of the matrix2a clast and the matrix2b. o) BSE image of Camp2a porphyroclast with the thin overgrowth of Camp2b equilibrated with Bt2b. p) X-ray elemental map showing distribution of Ca in Grt2a porphyroclast which is also surrounded in some parts by a thin overgrowth of Grt2b.

989

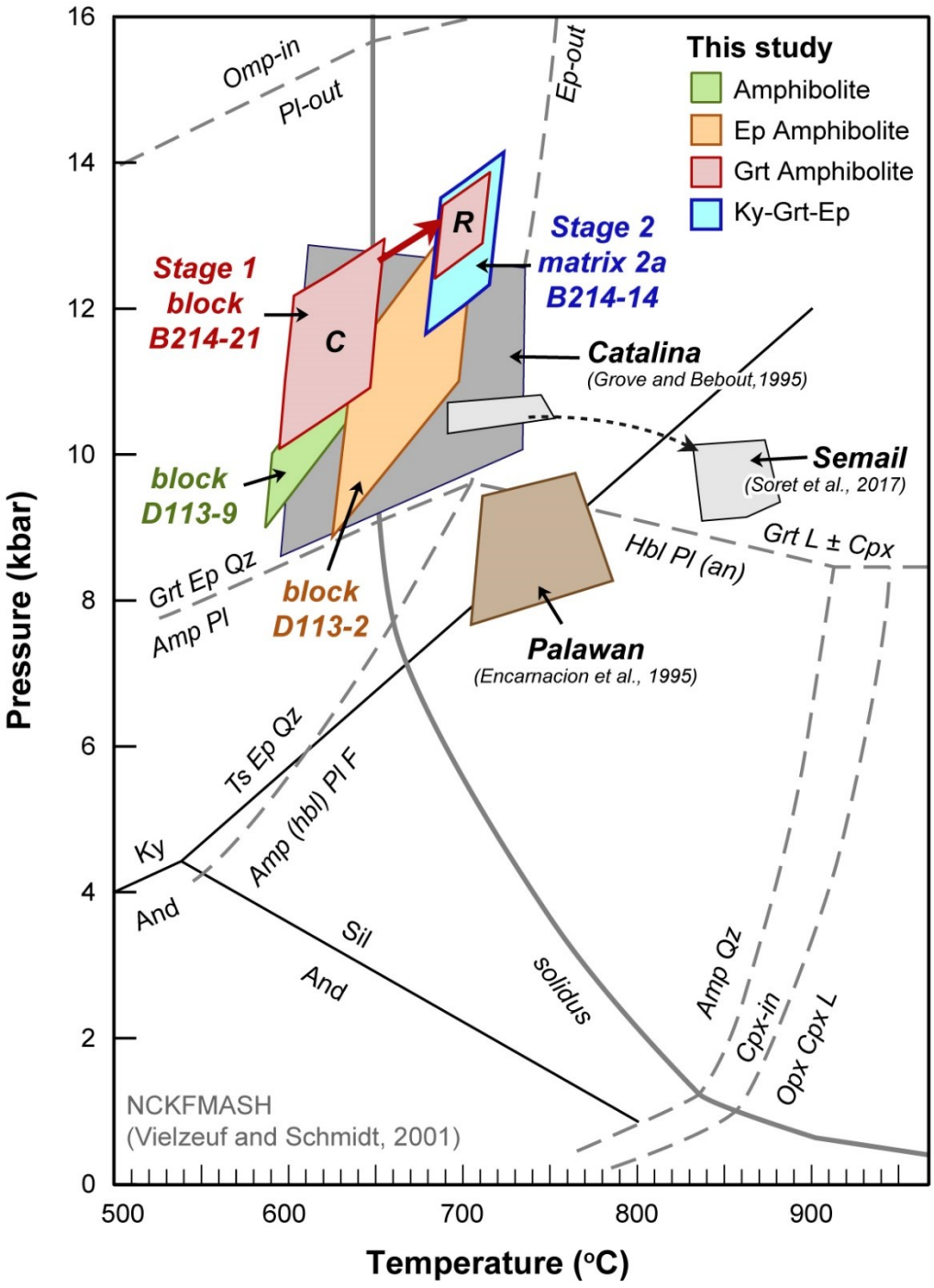

Fig. 9. *P-T* estimates for the blocks and matrix2a samples of the Dalrymple Amphibolite. The prograde *P-T* path for the Grt amphibolite block B214-21 was obtained using the inclusion assemblage (Zr-in-rutile geothermometry and quartz-in-garnet geobarometry) at the core (C) and rim (R) of garnet. The estimates for the amphibolite D113-9 and Ep amphibolite blocks D113-2 were determined using Zr-in-rutile geothermometry and the TZARS equilibria. *P-T* conditions of the matrix2a sample B214-14 utilized the same technique as in B214-21. See text for details. The peak *P-T* estimates for the Catalina Schist (Grove and Bebout, 1995) and the Semail Ophiolite (Soret et al., 2017) are also indicated. The petrogenetic grid for metabasalts in the NCKFMASH system (Vielzeuf and Schmidt, 2001) is also shown.

990

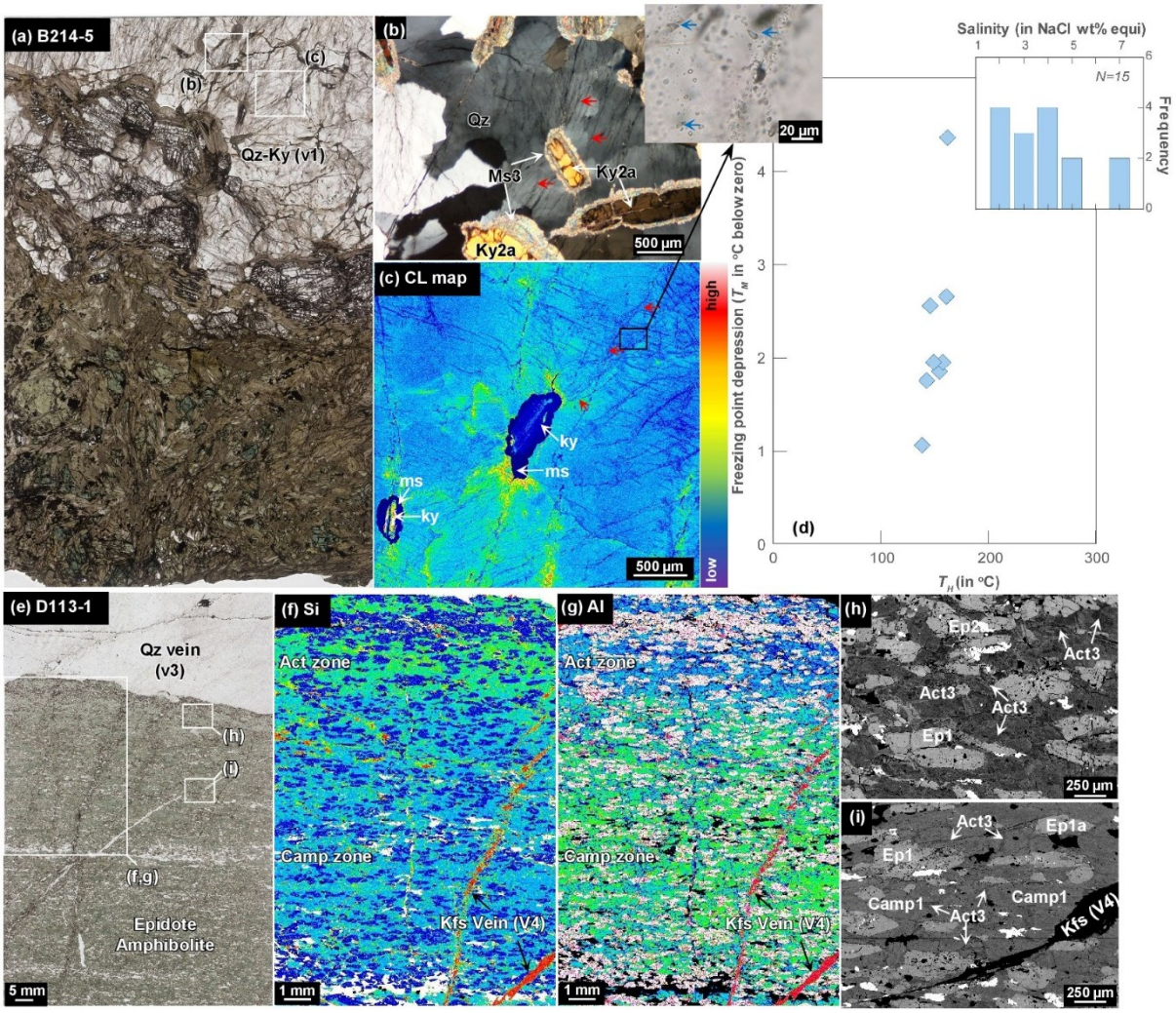

Fig. 10. a, b) Photomicrographs of Qz-Ky (B214-5) lens in matrix2a. The Ky2a grains replaced by Ms3 are interconnected by radial fractures (red arrows) that contain fluid inclusion (blue arrows). c) SEM-CL map of Qz-Ky lens. The fractures interconnecting the altered kyanite appear as thin nonluminescent lines marked by red arrows. Inset shows the fluid inclusions contained in these healed fractures. d) Homogenization (T_H) and melting (T_M) temperatures of the fluid inclusions. Histogram shows the salinity of these fluid inclusions calculated using Bodnar (1993). e) Scanned thin section of the Ep amphibolite sample in Dalrymple cut by a Stage 3 (v3) quartz vein. X-ray elemental maps reveal increasing f) Si and decreasing g) Al in the amphiboles towards the vein. BSE images show h) pervasive replacement of Camp1 (hornblende) by actinolite closer to the vein while replacement is limited i) along grain boundaries farther from the vein.

991

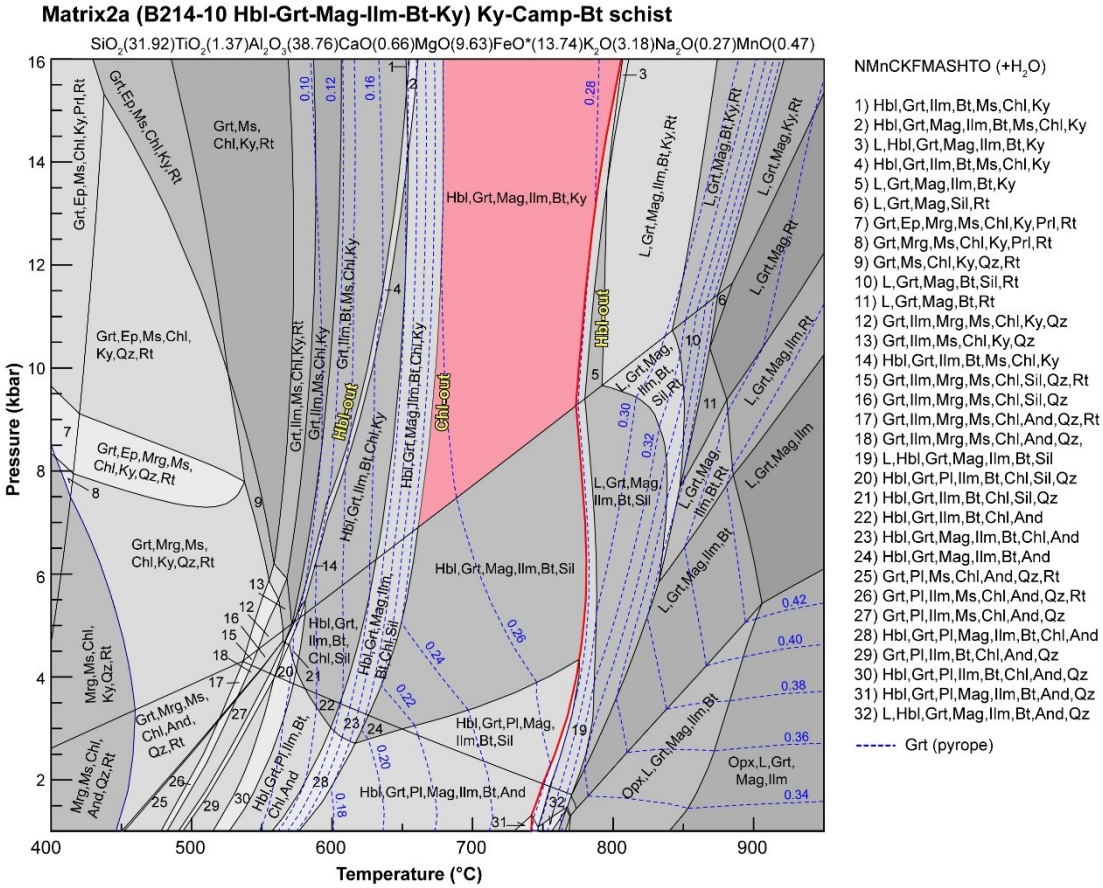

Fig. 11. Pseudosection calculated for the representative matrix2a sample B214-10 in the NMnCKFMASHTO system using Theriak-Domino (de Capitani and Brown, 1987; de Capitani and Petrakakis, 2010). Bulk rock composition used for the calculation is in molar percentages (%). Red field corresponds to the peak *P-T* assemblage observed in the samples while the solid red line is the calculated solidus. Isopleths of pyrope content (XPrp) of garnet are shown as blue dash lines.

992

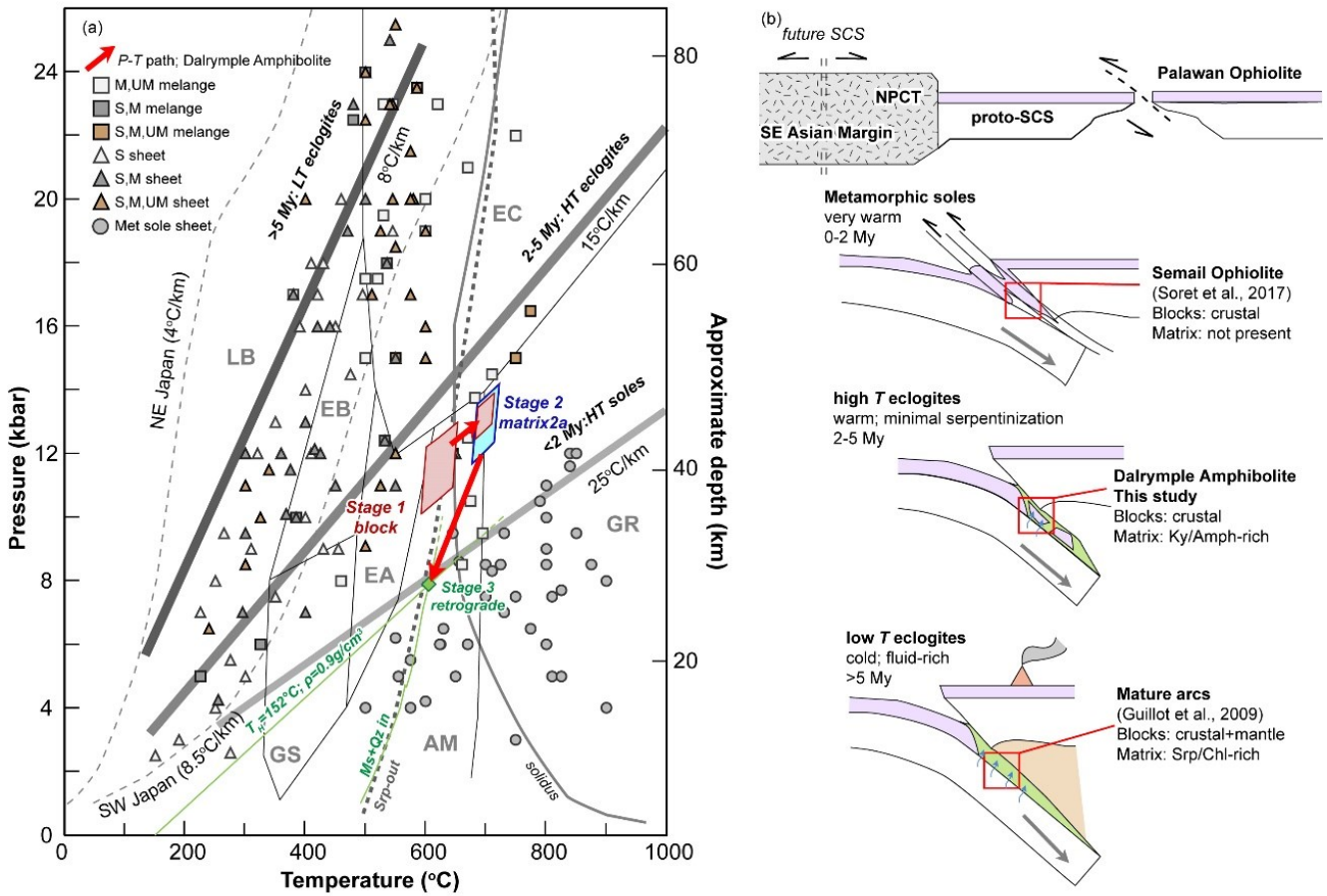

Fig. 12. a) *P-T* estimates for the Grt amphibolite block (Stage 1) and matrix2a (Stage2). The green diamond corresponds to the intersection of the isochore of the Stage 3 fluid inclusions and the calculated Ms+Qz-in curve for the matrix2a. Geothermal gradients of hot (SW Japan) and cold (NE Japan) subduction zones are from Peacock and Wang (1999). Metamorphic facies are from Guillot et al. (2009): LB-lawsonite blueschist, EB-epidote blueschist, EC-eclogite, GS-greenschist, EA-epidote amphibolite, AM-amphibolite, GR-granulite. Srp-out curve is from Ulmer and Trommsdorff (1995). Compilation of *P-T* conditions of metamorphic soles (met sole sheet) are from Agard et al. (2016) and other slab-mantle wedge interface lithologies (sheets and mélanges) are from Agard et al. (2018). The rock types that comprise each deposit are labelled M-mafic, UM-ultramafic, S-sedimentary. b) Schematic representation of the subduction initiation of the proto-South China Sea (SCS) promoted by the rifting of the North Palawan Continental Terrane (NPCT) from the southeast (SE) Asian Margin in the Eocene. The cooler paleogeothermal gradient preserved in the Dalrymple Amphibolite and its mélange occurrence resemble the transitional stage of subduction zones compared to metamorphic soles (e.g. Semail; Soret et al., 2017) and mature arcs (e.g. Guillot et al., 2009) as discussed in Agard et al. (2018). Blue arrows correspond to fluids released from the slab.

Table 1 Summary of samples used in this study

Sample No.	Locality			Field occurrence	Lithology	Major mineral assemblage [+secondary]	Accessory minerals	EPMA analysis	Notes
	Area	Latitude (N)	Longitude (E)						
B213-8	Botoon	10°8'7.1"	118°48'47.7"	Block	Grt amphibolite	Camp + Grt + Qz + Ep [+Chl +Ep]	Rt + Ilm + Zrn + Ap + Ky	○	
B214-2G	Botoon	10°7'44.2"	118°48'40.2"	Matrix2a	Grt amphibolite	Camp + Grt + Ky + St + Bt [+Chl]	Rt + Ilm + Zrn + Ap + Chl	○	
B214-5	Botoon	10°7'44.8"	118°48'40.6"	Qz-Ky lens in Matrix2a	Ky-Camp-Bt schist	Camp + Ky + St + Bt [+Chl +Ms]	Ilm	○	Stage 3 *P-T* estimation
B214-6	Botoon	10°7'44.8"	118°48'40.4"	Matrix2a	Ky-Grt-Bt schist	Grt + Ky + Ilm + Bt [+Chl +Ms]	Ap	○	
B214-8	Botoon	10°7'44.4"	118°48'40.6"	Matrix2a and 2b	Ky-Camp-Bt schist	Matrix2a: Camp + Oam + Grt + Ilm + Ky + Chl + Bt [+Chl] Matrix2b: Camp + Oam + Ilm + Ky+ Bt [+Ms +Chl]	Both 2a and 2b: Ap	○	
B214-9	Botoon	10°7'44.4"	118°48'40.6"	Matrix2a	Ky-Grt-Bt schist	Grt + Ky + Ilm + Bt [+Ms +Chl]	Ap	○	
B214-10	Botoon	10°7'44.7"	118°48'41"	Matrix2a	Ky-Camp-Bt schist	Camp + Grt + Ky + Ilm + Bt [+Ms +Chl]	Mag + Ap + Tur	○	Pseudosection
B214-14	Botoon	10°7'45.8"	118°48'41"	Matrix2a	Ky-Ep-Grt schist	Ky + Grt + Ep + Ilm + Bt [+Ms +Ep +Chl]	Rt + Ap + Zrn + Chl	○	Geothermobarometry
B214-21	Botoon	10°7'45.0"	118°48'40.1"	Block	Grt amphibolite	Camp + Grt + Ep + Qz [+Act +Ep +Chl]	Ky + Bt + Ap + Rt + Ilm + Zrn	○	Geothermobarometry cut by Qz-Ky vein
B214-29	Botoon	10°7'44.6"	118°48'40.8"	Matrix2a and 2b	Ky-Hbl schist	Matrix2a: Camp + Oam + Qz + Ky + Chl [+Chl +Ms] Matrix2b: Camp + Oam + Qz +Ky [+Ms]	Both 2a and 2b: Ilm	○	
N215-3	Nanad	10°7'24.3"	118°48'26.1"	Matrix2a and 2b	Grt-Hbl-Bt schist	Matrix2a and 2b: Camp + Grt + Ky + Bt + Qz [+Ms +Chl]	Ilm + Rt + Zrn + Ap	○	

Table 1 continued

Sample No.	Locality			Field occurrence	Lithology	Major mineral assemblage [+secondary]	Accessory minerals	EPMA analysis	Notes
	Area	Latitude (N)	Longitude (E)						
D113-1	Dalrymple	10°6'39.4"	118°48'41.1"	Block	Ep amphibolite	Camp + Ep + Pl + Qz [+Act +Chl +Ab]	Ttn + Ap	○	cut by Qz vein
D113-2	Dalrymple	10°6'39.4"	118°48'41.1"	Block	Ep amphibolite	Camp + Ep + Pl (An_{8-14}) + Qz [+Act +Ab]	Rt + Zrn + Ttn + Ap + Bt	○	Geothermobarometry
D113-5	Dalrymple	10°6'39.4"	118°48'41.1"	Block	Ep amphibolite	Camp + Ep + Pl (An_{1-14})+ Qz [+Act +Ab]	Rt + Zrn + Ttn + Ap + Bt	○	
D113-8	Dalrymple	10°6'41.6"	118°48'36.7"	Block	Ep amphibolite	Camp + Ep + Pl (An_{16-27}) + Qz [+Act +Ab]	Rt + Zrn + Ttn + Ap + Bt	○	
D113-9	Dalrymple	10°6'41.6"	118°48'36.7"	Block	Amphibolite	Camp + Ep + Pl (An_{8-17}) + Qz [+Act +Chl +Ab]	Rt + Zrn + Ttn	○	Geothermobarometry
D113-10	Dalrymple	10°6'41.6"	118°48'36.7"	Block	Ep amphibolite	Camp + Ep + Pl (An_{1-14}) + Qz [+Chl +Ab]	Rt + Zrn + Ttn + Ap + Bt	○	
D113-11	Dalrymple	10°6'41.6"	118°48'36.7"	Block	Amphibolite	Camp + Ep + Pl (An_{1-11}) + Qz [+Act +Ab]	Rt + Zrn	○	
D113-14	Dalrymple	10°6'42.5"	118°48'36.1"	Block	Grt amphibolite	Camp + Grt + Pl (An_{7-16}) + Qz + Ep [+Act +Chl +Ep]	Rt + Zrn + Ap + Ms	○	Geothermobarometry
D113-15	Dalrymple	10°6'42.5"	118°48'36.1"	Block	Grt amphibolite	Camp + Grt + Pl (An_{15-24}) + Qz + Ep [+Chl +Ep +Ab]	Rt + Ap + Ms + Ccp + Py	○	
D113-18	Dalrymple	10°6'43.3"	118°48'36.3"	Block	Grt amphibolite	Camp + Grt + Pl (An_{8-18}) + Qz + Ep + Bt [+Act +Chl +Ep +Ab]	Rt + Zrn + Ap	○	Geothermobarometry
D215-7	Dalrymple	10°6'43.3"	118°48'36.3"	Block	Ep-Bt-Ms schist	Bt + Ms + Pl + Ep +Qz [+Chl]	Rt + Ilm + Zrn + Ap	○	

993

994 Table 2. Summary of the mineral paragenesis, their representative mineral chemistry and the deformation (D) and veining (V) stages of the Dalrymple Amphibolite.

Phase	Block (Stage 1)*		Matrix (Stage 2)		Retrograde (Stage 3)
	Stage 1a	Stage 1b	Matrix 2a	Matrix 2b	
	D1	V1	D2a	V2 D2b	D3 V3
Grt	$Alm_{46-51}Prp_{10-19}Grs_{15-20}Sps_{15-25}$	$Alm_{38-41}Prp_{30-35}Grs_{13-15}Sps_{13-17}$	$Alm_{35-36}Prp_{28-32}Grs_{16-19}Sps_{16-19}$		
Amp		Camp1b: Mg# = 0.64-0.80	Oam2a/Camp2a: Mg# = 0.72-0.76	Oam2b/Camp2b: Mg# = 0.72-0.74	Camp3: Mg# = 0.45-0.83
Ep	Czo1a: Ps_{20-29}		Czo2a:Ps_{18-29} / Aln2a		Czo3: Ps_{30-39}
Pl		**An_{10-18}			An_{0-10}
Bt			Mg# = 0.80-0.86	Mg# = 0.75-0.81	
Rt	Nb = 175-266 ppm; Zr = 170-466 ppm	Nb = 720-5606 ppm; Zr = 222-562 ppm	Nb = 748-1782 ppm; Zr = 281-533 ppm		
Qz					
Ap					
Ilm					
Ky			Cr_2O_3 = 0.71-2.17 wt.%	Cr_2O_3 = 0.01-0.67 wt.%	
Chl			Mg# = 0.83-0.84		Mg# = 0.38-0.53
Ms					Si = 3.71-3.95 a.p.f.u.
Mag					
St					
Tur					

━━ - abundant **——** - accessory mineral **- - -** - minor minerals with special occurrence (see text for details)

*Mineral paragenesis of the Grt amphibolite block B214-21 used for geothermobarometry

**Pl1b is absent in Grt amphibolite block B214-21 but occurs in other Dalrymple Point blocks; Mineral chemistry data from D113-18

Table 3 Representative analyses of rock-forming minerals in the blocks

Sample No. (area)	B214-21 (Botoon)				D113-15 (Dalrymple)				
Lithology	Grt amphibolite				Grt amphibolite				
Mineral	Grt1		Hbl1		Grt1	Hbl1	Pl1	Ms1	Ep1
Occurrence	Matrix	Matrix	Matrix	Matrix	Matrix	Matrix	Matrix	Matrix	Matrix
Core/Mantle/Rim	Core	Rim	Core	Rim	Rim	Rim	Rim		
SiO_2	38.27	38.95	43.46	43.92	38.87	43.02	64.20	47.78	38.36
TiO_2	0.16	0.10	0.52	0.96	0.20	0.33	0.04	0.58	b.d.
Al_2O_3	20.94	21.60	15.13	14.94	21.31	14.80	22.83	30.94	23.62
Cr_2O_3	b.d.	0.03	0.02	0.04	0.02	b.d.	b.d.	b.d.	b.d.
FeO	22.46	19.55	12.03	11.11	26.74	17.47	b.d.	3.29	
Fe_2O_3									12.691
MnO	8.99	7.27	0.60	0.62	3.38	0.22	b.d.	0.04	0.10
MgO	3.17	7.71	12.22	12.44	4.28	8.82	b.d.	1.35	b.d.
CaO	6.53	5.07	10.57	10.92	6.84	10.34	4.36	0.03	23.72
BaO	n.d.	n.d.	0.01	0.09	0.04	0.02	0.04	0.24	b.d.
Na_2O	b.d.	0.07	1.80	1.71	0.06	2.69	9.06	1.33	b.d.
K_2O	0.02	b.d.	0.48	0.46	0.02	0.45	0.08	9.51	b.d.
F	n.d.	n.d.	0.09	0.08	b.d.	0.07	n.d.	b.d.	b.d.
Cl	n.d.	n.d.	b.d.	b.d.	b.d.	b.d.	n.d.	b.d.	b.d.
-O≡F			0.04	0.03		0.03			
-O≡Cl									
Total	100.53	100.36	96.92	97.30	101.75	98.21	100.62	95.10	98.49
Number of O	12	12	23	23	12	23	8	11	12.5
Si	3.02	3.00	6.32	6.37	3.01	6.39	2.82	3.22	3.03
Ti	0.01	0.01	0.06	0.10	0.01	0.04	<0.01	0.03	b.d.
Al	1.95	1.96	2.60	2.55	1.95	2.59	1.18	2.45	2.20
Cr	b.d.	<0.01	<0.01	<0.01	<0.01	<0.01	b.d.	b.d.	b.d.
Fe^{2+}	1.48	1.22	1.46	1.35	1.73	2.10	b.d.	0.19	
Fe^{3+}	<0.01	0.04	0.41	0.24	<0.01	0.07			0.75
Mn	0.60	0.47	0.07	0.08	0.22	0.03	b.d.	<0.01	0.01
Mg	0.37	0.89	2.65	2.69	0.49	1.95	b.d.	0.14	b.d.
Ca	0.55	0.42	1.65	1.70	0.57	1.65	0.21	<0.01	2.01
Ba			<0.01	<0.01	<0.01	<0.01	<0.01	0.01	b.d.
Na	b.d.	0.01	0.51	0.48	<0.01	0.77	0.77	0.17	b.d.
K	<0.01	b.d.	0.09	0.09	<0.01	0.09	<0.01	0.82	b.d.
F			0.04	0.04	b.d.	0.03		b.d.	b.d.
Cl			b.d.	b.d.	b.d.	b.d.		b.d.	b.d.
Total cation	7.99	8.01	15.86	15.69	8.00	15.71	4.98	7.02	7.99
$Mg/(Mg+Fe^{2+})$	0.20	0.42	0.64	0.67	0.22	0.48			
Prp	12.4	29.5			16.4				
Grs	18.4	13.9			18.8				
Sps	20.0	15.8			7.4				
Alm	49.3	40.7			57.4				
An							20.9		
Ps									25.5

b.d.=below detection limit; n.d.=not determined

Table 3 continued

Sample No. (area)	D113-9 (Dalrymple)					D113-2 (Dalrymple)		
Lithology	Amphibolite					Ep Amphibolite		
Mineral	Hbl1	Hbl3	Pl1	Ep1	Chl3	Hbl1	Pl1	Ep1
Occurrence	Matrix	Hbl alt	Matrix	Matrix	Hbl alt	Matrix	Matrix	Matrix
Core/Mantle/Rim	Rim	Rim	Rim	Rim		Rim	Rim	Rim
SiO_2	47.68	51.54	64.97	38.62	27.33	45.08	65.03	38.17
TiO_2	0.43	0.07	b.d.	b.d.	0.03	0.82	b.d.	0.17
Al_2O_3	11.91	2.95	22.23	25.58	22.07	11.64	22.14	23.94
Cr_2O_3	0.11	0.05	b.d.	0.05	0.13	0.07	0.01	b.d.
FeO	10.28	20.31	b.d.		12.65	14.28	0.13	
Fe_2O_3				10.355				12.618
MnO	0.37	0.40	b.d.	0.17	0.23	0.21	b.d.	0.10
MgO	13.96	9.22	0.02	0.05	23.17	12.11	0.03	0.06
CaO	11.24	11.94	3.01	23.66	b.d.	10.22	3.05	23.34
BaO	0.03	b.d.	b.d.	0.06	b.d.	0.18	0.06	0.08
Na_2O	1.90	0.52	10.31	b.d.	0.02	2.58	10.34	b.d.
K_2O	0.21	0.28	0.10	b.d.	0.01	1.27	0.09	b.d.
F	b.d.	0.01	n.d.	0.04	0.01	0.14	n.d.	0.01
Cl	0.01	0.01	n.d.	b.d.	0.01	b.d.	n.d.	<0.01
-O≡F		0.00		0.01	0.00	0.06		0.01
-O≡Cl	0.00	0.00			0.00			0.00
Total	98.14	97.28	100.64	98.57	85.65	98.61	100.86	98.50
Number of O	23	23	8	12.5	28	23	8	12.5
Si	6.81	7.75	2.85	3.02	5.50	6.62	2.85	3.01
Ti	0.05	0.01	b.d.	b.d.	<0.01	0.09	b.d.	0.01
Al	2.01	0.52	1.15	2.36	5.23	2.02	1.14	2.23
Cr	0.01	<0.01	b.d.	<0.01	0.01	<0.01	<0.01	b.d.
Fe^{2+}	1.23	2.55	b.d.		2.13	1.75	<0.01	
Fe^{3+}	<0.01	<0.01		0.61		<0.01		0.75
Mn	0.05	0.05	b.d.	0.01	0.04	0.03	b.d.	0.01
Mg	2.97	2.07	<0.01	0.01	6.95	2.65	<0.01	0.01
Ca	1.72	1.92	0.14	1.98	b.d.	1.61	0.14	1.97
Ba	<0.01	b.d.	b.d.	<0.01	b.d.	0.01	<0.01	<0.01
Na	0.53	0.15	0.88	b.d.	0.01	0.74	0.88	b.d.
K	0.04	0.05	0.01	b.d.	<0.01	0.24	<0.01	b.d.
F	b.d.	<0.01		0.01	0.01	0.07		<0.01
Cl	<0.01	<0.01		b.d.	<0.01	b.d.		<0.01
Total cation	15.41	15.08	5.02	8.00	19.87	15.82	5.02	7.99
$Mg/(Mg+Fe^{2+})$	0.71	0.45			0.77	0.60		
Prp								
Grs								
Sps								
Alm								
An			13.8				13.9	
Ps				20.5				25.2

b.d.=below detection limit; n.d.=not determined

Table 4 continued

Sample No. (area)	B214-14 (Botoon)			B214-29 (Botoon)					
Lithology	Ky-Ep-Grt schist			Ky-Hbl schist					
Mineral	Grt2a		Ep2a	Hbl2a	Oam2a	Ky2a	Hbl2b	Oam2b	Ky2b
Occurrence	Ky inclusion		Matrix	Matrix	Matrix	Matrix	Matrix	Matrix	Matrix
Core/Mantle/Rim	Core	Rim	Rim	Rim		Rim	Rim		
SiO_2	39.50	39.91	30.38	44.88	47.66	36.85	45.11	48.57	37.10
TiO_2	0.35	0.10	35.23	0.22	b.d.	0.14	0.37	0.11	b.d.
Al_2O_3	21.22	21.79	1.95	13.55	13.98	59.91	14.34	13.06	60.87
Cr_2O_3	b.d.	b.d.	b.d.	0.98	0.64	1.85	0.05	b.d.	0.67
FeO	17.35	16.58		9.59	11.39		8.85	11.73	
Fe_2O_3			1.19			1.98			1.39
MnO	7.34	6.93	0.18	0.62	1.03	0.04	0.56	1.09	0.05
MgO	8.12	8.07	b.d.	14.39	19.86	0.02	14.69	21.38	0.02
CaO	6.26	6.84	28.98	9.95	0.69	0.02	10.12	0.68	b.d.
BaO	n.d.	n.d.	0.08	0.09	b.d.	0.09	b.d.	b.d.	b.d.
Na_2O	n.d.	n.d.	0.05	1.81	1.19	b.d.	2.04	1.37	0.01
K_2O	n.d.	n.d.	0.03	0.27	b.d.	b.d.	0.26	b.d.	0.01
F	n.d.	n.d.	0.03	0.04	0.12	0.03	0.10	b.d.	b.d.
Cl	n.d.	n.d.	b.d.	<0.01	b.d.	b.d.	0.01	b.d.	b.d.
-O≡F			0.01	0.02	0.05	0.01	0.04		
-O≡Cl				0.00			0.00		
Total	100.14	100.21	98.10	96.38	96.55	100.93	96.48	97.99	100.10
Number of O	12	12	12.5	23	23	20	23	23	20
Si	3.03	3.04	2.53	6.49	6.74	4.00	6.47	6.77	4.03
Ti	0.02	0.01	2.21	0.02	<0.01	0.01	0.04	0.01	b.d.
Al	1.92	1.96	0.19	2.31	2.33	7.66	2.42	2.14	7.79
Cr	b.d.	b.d.	b.d.	0.06	0.04	0.08	<0.01	b.d.	0.03
Fe^{2+}	1.11	1.06		1.16	1.35		1.06	1.37	
Fe^{3+}	<0.01	<0.01	0.07	0.36	<0.01	0.16	0.40	<0.01	0.11
Mn	0.48	0.45	0.01	0.08	0.12	<0.01	0.07	0.13	<0.01
Mg	0.93	0.92	b.d.	3.10	4.19	<0.01	3.14	4.44	<0.01
Ca	0.51	0.56	2.59	1.54	0.10	<0.01	1.56	0.10	b.d.
Ba			<0.01	0.01	b.d.	<0.01	b.d.	b.d.	b.d.
Na			0.01	0.51	0.33	b.d.	0.57	0.37	<0.01
K			<0.01	0.05	b.d.	b.d.	0.05	b.d.	<0.01
F			0.01	0.02	0.05	0.01	0.05	b.d.	b.d.
Cl			b.d.	<0.01	b.d.	b.d.	<0.01	b.d.	b.d.
Total cation	7.99	7.98	7.64	15.70	15.24	11.93	15.82	15.33	11.97
$Mg/(Mg+Fe^{2+})$	0.45	0.46		0.73	0.76		0.75	0.76	
Ps			28.0						

b.d.=below detection limit; n.d.=not determined

996

Table 4 Representative analyses of rock-forming minerals in the matrix

Sample No. (area)	N215-3 (Nanad)					
Lithology	Grt-Hbl-Bt schist					
Mineral	Hbl2a	Bt2a	Bt2b	Bt3	Ms3	Chl3
Occurrence	Porphyroclast		Matrix	Matrix	Matrix	Matrix
Core/Mantle/Rim	Rim					
SiO_2	45.96	40.97	40.45	40.55	49.37	28.16
TiO_2	0.30	0.87	1.06	1.03	0.66	0.18
Al_2O_3	13.67	17.51	16.91	16.52	30.40	21.45
Cr_2O_3	0.13	b.d.	0.27	0.13	0.05	0.19
FeO	10.39	9.55	9.74	9.42	3.89	9.77
Fe_2O_3						
MnO	0.63	0.27	0.32	0.36	0.03	0.41
MgO	14.13	17.03	17.04	17.27	2.52	25.44
CaO	9.02	0.10	0.03	0.03	0.03	b.d.
BaO	b.d.	0.14	0.23	0.03	0.19	0.06
Na_2O	3.23	0.38	0.15	0.14	0.73	b.d.
K_2O	0.23	7.85	8.58	8.45	6.07	b.d.
F	b.d.	0.15	b.d.	0.16	0.12	0.01
Cl	b.d.	b.d.	b.d.	0.01	<0.01	0.01
-O≡F		0.06		0.07	0.05	0.00
-O≡Cl				0.00	0.00	0.00
Total	97.68	94.82	94.77	94.10	94.06	85.67
Number of O	23	11	11	11	11	28
Si	6.59	2.94	2.92	2.94	3.29	5.58
Ti	0.03	0.05	0.06	0.06	0.03	0.03
Al	2.31	1.48	1.44	1.41	2.38	5.01
Cr	0.01	<0.01	0.01	<0.01	<0.01	0.01
Fe^{2+}	1.25	0.57	0.59	0.57	0.22	1.62
Fe^{3+}	0.11					
Mn	0.08	0.02	0.02	0.02	<0.01	0.07
Mg	3.02	1.82	1.84	1.87	0.25	7.52
Ca	1.39	0.01	<0.01	<0.01	<0.01	b.d.
Ba	b.d.	<0.01	0.01	<0.01	<0.01	<0.01
Na	0.90	0.05	0.02	0.02	0.09	b.d.
K	0.04	0.72	0.79	0.78	0.52	b.d.
F	b.d.	0.03	b.d.	0.04	0.03	<0.01
Cl	b.d.	b.d.	b.d.	<0.01	<0.01	<0.01
Total cation	15.73	7.69	7.69	7.73	6.82	19.86
$Mg/(Mg+Fe^{2+})$	0.71	0.76	0.76	0.77		0.82
Ps						

b.d.=below detection limit; n.d.=not determined

997